Towards Hourly 4-D Subsurface Monitoring using Seismic Ambient Noise

Peng Guo[1] and Erdinc Saygin[1]

[1]CSIRO

November 23, 2022

Abstract

We use seismic ambient noise recorded by ocean bottom nodes (OBNs) in the Gorgon gas field, Western Australia to compute time-lapse seafloor models. The extracted hourly cross-correlation (CC) functions of 0.1 – 1 Hz contain mainly Scholte waves with very high signal to noise ratio. The conventional time-lapse analysis suggests relative velocity variations (dv/v) up to 1% assuming a spatially homogeneous dv/v, with a likely 24-hour cycling pattern. With high-resolution baseline models from full waveform inversion of Scholte waves, we propose a double-difference waveform inversion (DD-WI) method using travel time differences for localizing the time-lapse dv/v in the heterogeneous subsurface in depth. The time-lapse velocity models show velocity increase/decrease patterns in agreement with that from conventional analysis, with more notable changes at the shallower depths. We demonstrate the feasibility of using ambient noise for quantitative monitoring of subsurface property changes in the horizontal and depth domain at an hourly basis.

Towards Hourly 4-D Subsurface Monitoring using Seismic Ambient Noise

Peng Guo[1,*] and Erdinc Saygin[1,2]

[1] Deep Earth Imaging Future Science Platform, The Commonwealth Scientific and Industrial Research Organisation (CSIRO), Kensington 6151, Western Australia, Australia.

[2] Department of Physics, School of Physics, Mathematics and Computing, Faculty of Engineering and Mathematical Sciences, University of Western Australia, Crawley 6009, Western Australia, Australia.

Corresponding author: Peng Guo (peng.guo@csiro.au)

Key Points:

- We present a new method for high-resolution 4-D passive monitoring of subsurface physical property.
- We compute hourly quantitative time-lapse images of velocity changes in the horizontal and depth domain from offshore ambient noise.
- The method opens new avenues for 4-D monitoring using ambient noise from dense arrays and DAS.

Abstract

We use seismic ambient noise recorded by the ocean bottom nodes (OBNs) in the Gorgon gas field, Western Australia to compute time-lapse seafloor models. The extracted hourly cross-correlation (CC) functions of 0.1 – 1 Hz contain mainly Scholte waves with very high signal to noise ratio. The conventional time-lapse analysis suggests relative velocity variations (dv/v) up to 1% assuming a spatially homogeneous dv/v, with a likely 24-hour cycling pattern. With high-resolution baseline models from full waveform inversion of Scholte waves, we propose a double-difference waveform inversion (DD-WI) method using travel time differences for localizing the time-lapse dv/v in the heterogeneous subsurface in depth. The time-lapse velocity models show velocity increase/decrease patterns in agreement with that from conventional analysis, with more notable changes at the shallower depths. We demonstrate the feasibility of using ambient noise for quantitative monitoring of subsurface property changes in the horizontal and depth domain at an hourly basis.

1 Introduction

Temporal variations of subsurface physical properties have been commonly observed, for example, within active volcanos and fault zones, natural resources (e.g., hydrocarbon, geothermal) production fields, and carbon/hydrogen capture/storage in rock reservoirs (Lumley, 2001; Brenguier et al., 2008; Takano et al., 2014; Roche et al., 2021). Seismic monitoring using environmental ambient noise (passive seismic data) has been demonstrated as a powerful and cost-effective solution for detecting and quantifying such property changes (Sens-Schönfelder and Wegler, 2006). A simple cross-correlation (CC) of ambient noise wavefield recorded at two receivers reconstructs the virtual interstation Green's function, which can be interpreted as the seismic response that would be measured at one of the receiver locations as if there is a source at the other location (e.g., Shapiro and Campillo, 2004). The ever-present natural ambient sources enable continuous and reliable retrievals of the seismic responses between pairs of stations across times, for example at a daily (de Ridder and Biondi, 2013) or hourly basis (Mao et al., 2019); the waveform changes (e.g., the travel time shifts) from the time-lapse CC functions can be used for deriving the temporal variations of seismic velocity (dv/v) (Richter et al., 2014). Compared with expensive controlled-source seismic survey for time-lapse monitoring (Hicks et al., 2016), seismic monitoring using ambient noise helps reduce the operational cost significantly and is also environmentally friendly; it is also preferred to monitoring methods using nature-sourced earthquakes because of the lack of repeatability and universal distribution for the latter (Kamei and Lumley, 2017).

Previous studies suggest that seismic ambient noise is mainly originated from the interaction of the ocean with the solid earth (Stehly et al., 2006; Gualtieri et al., 2020). The main signals extracted from seismic ambient noise are usually surface waves (e.g., Shapiro and Campillo, 2004; Stehly et al., 2006; Brenguier et al., 2016), albeit body waves have also been observed (e.g., Roux et al., 2005; Nakata et al., 2016; Saygin et al., 2017). Both the coda part and direct (ballistic) arrivals of the extracted seismic responses have been used for monitoring and can be sensitive to minor velocity changes at the order of 0.1% (Sens-Schönfelder and Wegler, 2006; Brenguier et al., 2020; Takano et al., 2020). It is of common practice for seismic passive monitoring to detect the temporal changes with a spatially homogeneous change assumption (Sens-Schönfelder and Wegler, 2006), however it remains challenging to characterize their detailed spatial distribution. There have been studies using ballistic surface wave arrivals (de Ridder and Biondi, 2013; de Ridder et al., 2014; Mordret et al., 2014) that localize the velocity changes in the horizontal plane but without determining the depth extent, and using the eikonal equation for describing the physics which is less accurate than inversion methods based on the elastic-wave equation. Mordret et al. (2020) estimate velocity changes in depth from dispersion measurements however with a 1-D assumption. The spatial extent of changes has also been determined using coda sensitivity kernels (Obermann et al., 2013; Rodríguez Tribaldos et al., 2021) but the resolution is relatively low. Compared with the established workflows for determining quantitative 4-D (space-time) models of temporal velocity changes using body waves from controlled seismic sources (e.g., Lumley, 2001; Zhang & Huang, 2013; Yang et al., 2016; Hicks et al., 2016), there has been a significant knowledge gap for subsurface real-time monitoring using surface waves from ambient noise.

Seismic monitoring using ambient noise has great potential for industrial applications, including the real-time monitoring of carbon/hydrogen geological storage in subsurface rock reservoirs for the ongoing decarbonization efforts. We present a study for spatio-temporal monitoring of the subsurface heterogeneous physical property changes using offshore seismic ambient noise. We extract hourly Scholte wave of 0.1 – 1 Hz from two-day seafloor seismic noise recorded by the vertical component of ocean bottom nodes (OBNs). Time-lapse analysis shows temporal changes of the seafloor velocity (dv/v) up to ~1%. With a baseline seafloor model from FWI of Scholte waves, we propose a double-difference waveform inversion (DD-WI) method using differential arrival times for estimating high-resolution time-lapse velocity models. Synthetic and field data studies show that it is feasible for 4-D real-time quantitative monitoring using ambient noise, i.e., detecting and localizing subtle subsurface velocity changes in the horizontal and depth domain at an hourly basis using ambient noise data from dense arrays.

2 Data and ambient noise interferometry

Between 2015 and 2016, Chevron Australia and its partners acquired a 3-D OBN seismic survey over the Gorgon gas field for a better description of the Gorgon reservoir sands for carbon capture and storage, with the survey area located in the North West Shelf offshore of Western Australia, approximately 200 km from the mainland (Fig. 1a and 1b). Both the in-line and cross-line intervals were 375 m, with 120 OBN lines covering an area of ~ 436 km^2. The inline direction was 115^o/295^o, about perpendicular to the coastal line. The water depth in the survey region was between 200 - 600 m. Each node comprised four channels, with two horizontal components (X, Y) and one vertical component (Z) for measuring displacement, and a hydrophone component for recording pressure. The data were recorded continuously with a 2 millisecond interval. The survey used controlled air-gun seismic sources, but there were several quiet time windows without using controlled active sources. The recorded ambient seismic wavefield in the absence of active seismic sources provides the opportunity for passive seismic monitoring using a dense seismic array of industrial scale. We select a time window of Julian Days 1 and 2 of 2016 for the passive seismic monitoring experiment.

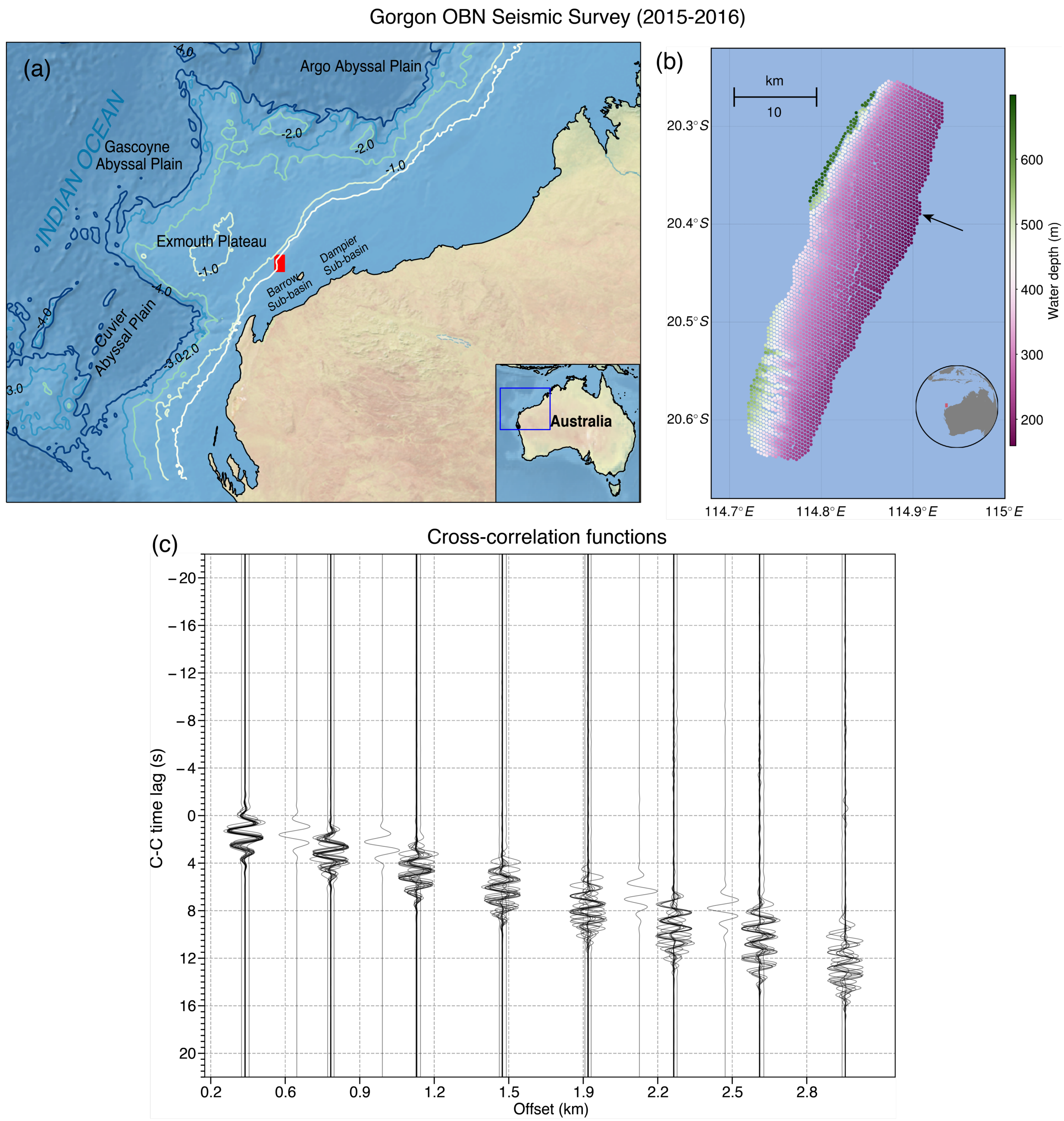

Fig. 1. Map of the ocean bottom seismic survey in Western Australia and cross-correlation (CC) functions from ambient noise interferometry. (a) Ocean Bottom Node (OBN) seismic survey in the Gorgon gas field offshore Western Australia by Chevron Australia and its partners. (b) Zoom-in of the red rectangle in (a), with the color on the OBNs suggesting water depths; the black arrow indicates Line 3924. (c) CC functions for Line 3924 sorted by offsets (the distance between stations of a station pair) from Hour 15 of Julian Day 1, 2016. We limit the CC functions to 3 km.

We detrend and down-sample the vertical component of the data from 250 Hz to 20 Hz with anti-aliasing filtering. The ambient noise data are then filtered at 0.1 – 1 Hz. We divide the recordings of the selected quiet time window without active source shooting into hour-long segments; each segment is then subdivided into 30 s long records with a 50% overlap. Green's functions are reconstructed by computing CC functions of the 30 s ambient noise window between station pairs. We use weighted phase stacking (Schimmel et al., 2011) for stacking the CC functions within each hour-long segment to improve the signal to noise ratio. Fig. 1c shows the CC functions at Hour 15 Day 1 for Line 3924 (indicated by the black arrow in Fig. 1b), which contain mainly Scholte waves (travelling along the interface between the seawater and seafloor) and provide constraints for the shear-wave velocity of the seafloor. The hourly extracted CC functions have a very high signal to noise ratio. The energy concentrates on the positive side of the CC time lags, suggesting that the ambient noise between 0.1 and 1 Hz propagates from the ocean to the coast.

3 Methods and results

3.1 Seismic velocity temporal monitoring

A baseline (reference) data for each station pair can be obtained by stacking the hourly CC functions across all the available hours from the two-day passive recordings. We compare the ballistic part of the Scholte wave arrivals of the baseline data with that of the hourly CC functions for quantifying the temporal velocity variations. The conventional time-lapse analysis using the stretching method assumes that the relative velocity variation (dv/v) is uniform in space, therefore we have the relation of dv/v with the relative travel time change (dt/t) as $dv/v=-dt/t$ (Sens-Schönfelder and Wegler, 2006). Fig. 2 shows the derived velocity changes across the two days. We notice that the seafloor velocity changes up to 1% (Fig. 2a), with a likely sinusoidal pattern of ~ 24-hour cycle. The smaller offsets, which provide constraints for the shallower depths, generally have larger velocity variations than those from the relatively larger offsets (Fig. 2b), which are more associated with the velocities at the greater depths. The velocity changes from Fig. 2 can be interpreted as the average velocity changes of the seafloor where the extracted Scholte waves propagate through. The temporal changes of velocities from more survey lines, as indicated by the black arrows in Fig. S1, are shown in Fig. S2, which suggests similar patterns of velocity temporal changes with Fig 2.

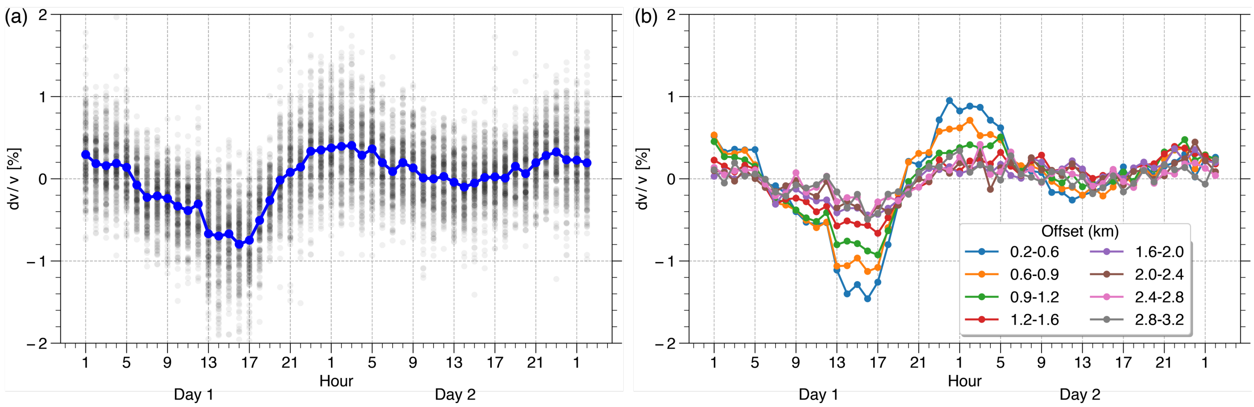

Fig. 2. The relative velocity temporal changes (dv/v) from the stretching method. (a) dv/v of the seafloor at an hourly basis for Julian Day 1 and Day 2 of 2016. The velocity changes were estimated from the ballistic part of the extracted Scholte waves in Line 3924. Each black dot is the dv/v from a station pair measurement. The blue curve is the average dv/v. (b) The average velocity changes from CC functions of different offset ranges, for example '0.2-0.6' refers to CC functions of 0.2 – 0.6 km offset.

We sort the CC functions of all the station pairs into common-station gathers. Each common-station gather can be considered as a seismic common-source gather that the shared common station is the source, and the rest of the stations from the selected survey line are the receivers. Fig. 3 contains common-station gathers of the baseline data and the monitoring data from Hour 15 of Day 1 (Fig. 3a) and Hour 1 of Day 2 (Fig. 3b). We observe that the main difference between the baseline and monitoring data of different hours are the arrival times of the Scholte waves. Scholte waves from Hour 15 of Day 1 arrive later than the baseline data (Fig. 3a, 3c), indicating a velocity decrease than the baseline model, while those from Hour 1 of Day 2 arrive at an earlier time than the baseline data (Fig. 3b, 3d), suggesting a velocity increase; these observations from the common-station gathers are consistent with Fig. 2.

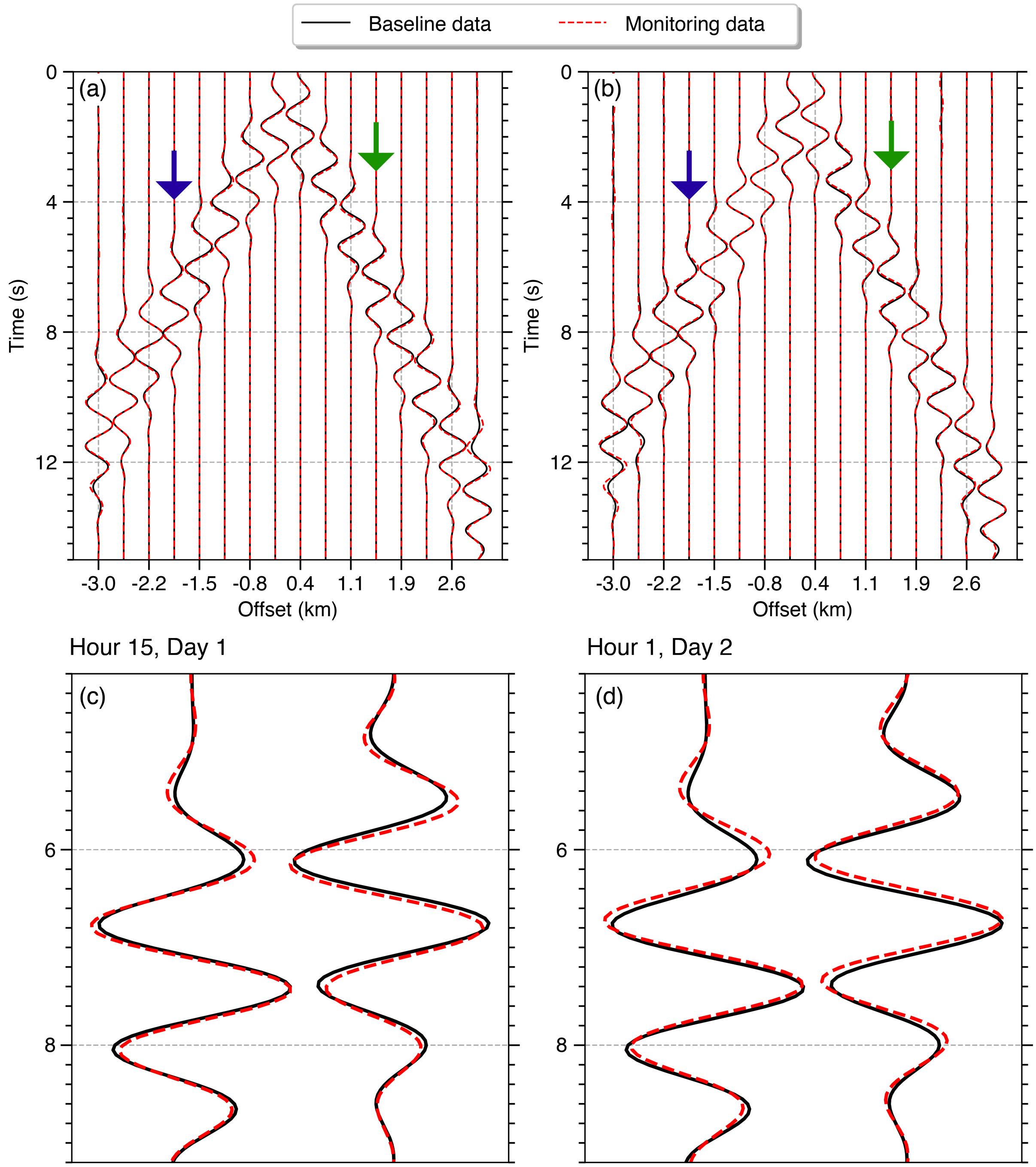

Fig. 3. Common-station gathers sorted from CC functions of station pairs of Line 3924. (a) is the comparison of the baseline data (solid black curve) and the monitoring data (dashed red curve) of Hour 15 Day 1. (b) is the comparison of the baseline data (solid black curve) and the monitoring data (dashed red curve) of Hour 1 Day 2. (c) and (d) are zoom-in of the seismic trace at -1.9 km and 1.5 km offsets (from left to right, indicated by the blue and green arrows, respectively) from (a) and (b).

3.2 Full waveform inversion for baseline model estimation

The dense array of OBNs provides the opportunity for computing time-lapse quantitative images of velocity changes, i.e., localizing the temporal velocity changes in the horizontal and depth domain of the subsurface, from the continuous recordings of ambient noise using high-resolution waveform inversion technique.

A baseline velocity model is necessary for comparing with the time-lapse subsurface models. We use the full waveform inversion (FWI) (Tarantola, 1984; Shipp & Singh, 2002; Guo et al., 2022) technique for estimating a high-resolution baseline model using the extracted Scholte waves. For its numerical implementation, a gradient-based linearized inversion approach is used for updating the velocity model iteratively in the aim of minimizing the misfit between synthetic and observed data, with the gradients of the data misfit to model parameters efficiently calculated by the adjoint-state method from the cross-correlation of the source and adjoint wavefields (Tarantola, 1984; Fichtner et al., 2006). The source and adjoint wavefields can be obtained by source-wavelet generated forward wave propagation and adjoint-source generated backward wave propagation (Shipp & Singh 2002). We use time-domain staggered-grid finite-difference (Virieux, 1986) with fourth-order spatial and second-order temporal accuracy for solving the elastic-wave equation in the stress and particle-velocity formulation.

We use the baseline data in the form of common-station gathers (e.g., Fig. 3) as the observed data for the baseline FWI. Considering that the phase information in the virtual Scholte waves of the CC functions is more reliable than the amplitude, here we use a trace-normalized FWI method (Shen, 2010) where each seismic trace is normalized by the l-2 norm of the trace itself in the misfit function (Text S1).

Fig. S3a shows the velocity model from the wave-equation dispersion inversion, which uses the adjoint-state method for fitting the surface wave dispersion spectra (Li et al. 2017; Chen & Saygin, 2022). With the model in Fig. S3a as the starting model, Fig. 4a shows the velocity model from the baseline trace-normalized FWI after 50 iterations. The data misfit has been much reduced after FWI (Fig. S4). The synthetically calculated data after the FWI show much better match (Fig. S5) to the extracted Scholte wave arrivals of the observed baseline data than those from the starting model. The velocity model in Fig. 4a is used as the baseline model for computing time-lapse seafloor models.

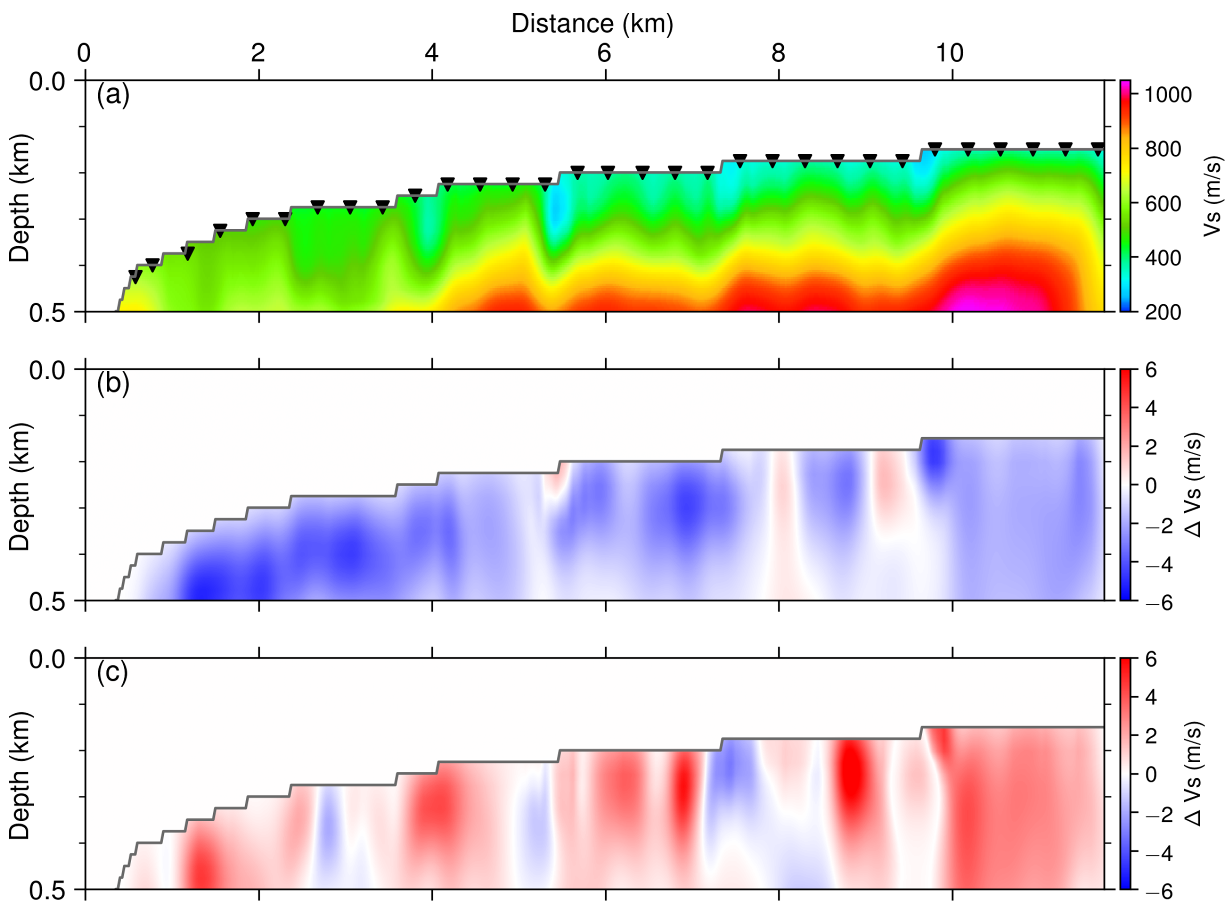

Fig. 4. Baseline velocity model and time-lapse subsurface models of velocity changes in the shallow seafloor. (a) The high-resolution baseline velocity model from trace-normalized FWI, which is used as the starting model for DD-WI. (b) The time-lapse image of velocity changes for Hour 15 Day 1. (c) The time-lapse image of velocity changes for Hour 1 Day 2. The black triangles in (a) indicate the locations of the OBNs.

3.3 Double-difference waveform inversion for localizing time-lapse velocity changes

The most straightforward approach for generalizing seismic inversion to the time-lapse monitoring is to perform two inversions for the baseline and the monitoring data respectively, however the results are sensitive to the baseline model and could be heavily contaminated by the residual data misfit from the baseline inversion (Yang et al., 2016). Double-difference waveform inversion (DD-

WI) (Denli and Huang, 2009) using differential waveforms has been used for providing more reliable subsurface models of velocity changes with body waves from controlled sources.

The time-lapse difference of the data mainly manifests in the travel times (Fig. 3), which suggests that an objective function of the seismic time-lapse inversion problem using travel time differences (shifts) between the monitoring and baseline data may be the most stable for quantifying the time-lapse velocity models. DD-WI using travel time differences as an objective function has been proposed before, but in the background of seismic adjoint tomography for estimating seismic wave velocity structures, where the differential measurements are constructed between receivers (Yuan et al., 2016). We introduce it for elastic-wave equation based time-lapse inversion where the differential measurements are constructed between baseline and monitoring data.

Here, we propose the DD-WI method using travel time differences for obtaining time-lapse velocity models using the extracted Scholte waves from ambient noise. The misfit function is defined as

$$J = \sum_{i=1}^{Ns} \sum_{j=1}^{Nr} \left\| \Delta t_{i,j}^{d} - \Delta t_{i,j}^{s} \right\|^2 \quad (1)$$

where $\Delta t_{i,j}^{d}$ is the travel time difference between the monitoring and the baseline observed data, and $\Delta t_{i,j}^{s}$ is the travel time difference between the synthetic data from the monitoring model and the baseline FWI model. i and j are the indexes for the sources and receivers, Ns and Nr are the number of sources and receivers. The time difference (shift) can be estimated by comparing waveform data using cross correlation. The term 'double-difference' comes from the two-level differences in equation 3: (1) the difference between baseline and monitoring data, either synthetic or observed, and (2) the difference between the synthetic and observed measurements from (1).

The adjoint source for the DD-WI of travel time differences (Yuan et al., 2016), which is used for elastic wave propagation in backward time steps for computing the adjoint wavefields, can be derived as

$$\chi_{i,j} = [\Delta t_{i,j}^{d} - \Delta t_{i,j}^{s}] \partial t \; s_{i,j} \; (t - \Delta t_{i,j}^{s}), \quad (2)$$

where $\boldsymbol{s_{i,j}}$ is a seismic waveform trace (1-D time-series vector) from the synthetic data. The only difference with the FWI is the adjoint source. Both the baseline and time-lapse inversion methods honor the seafloor bathymetry which is implicitly included when solving the elastic-wave equation. We apply the DD-WI method to the differential measurements of monitoring and baseline data for localizing the shear-wave velocity changes in the seafloor at an hourly basis. The misfit has been largely reduced after inversion (Fig. S6). The derived velocity difference between the model of Hour 15 Day 1 and the baseline model is shown in Fig. 4b, with that of Hour 1 Day 2 shown in Fig. 4c. The changes in Fig. 4b are overall negative suggesting a slower velocity than the baseline model, while the velocity differences in Fig. 4c are mainly positive indicating a faster velocity than the baseline; both are in agreement with Figs. 2 and 3. We also observe that the velocity changes are more significant at the shallower depths, up to ~1% relative to the baseline model, consistent with Fig. 2b where there are larger temporal velocity changes from the CC functions of smaller offsets (shallower depth) than those of the larger offsets (Fig. 2b). We estimate time-lapse models of velocity changes from more hours (Figs. S7, S8). We also apply the inversion method to the monitoring data from more survey lines (Figs. S9, S10); the localized time-lapse velocity changes of the seafloor show consistent increase/decrease patterns with Fig. S2.

4 Discussion

The observed temporal velocity changes (up to ~1%) is subtle, especially when compared with the likely difference between the baseline model from FWI and the ground truth of the seafloor. It is important to test if these velocity changes are real, not coming from the unfitted data in the baseline inversion. Therefore we perform a series of synthetic tests (Text S2, Fig. S11-S16), especially with errors in the baseline model and noise in the baseline and time-lapse data. The inversion results suggest that the proposed method is robust to data noise and errors in the baseline model, and the velocity temporal changes localized by DD-WI using differential travel times are reliable.

Surface wave or ambient noise tomography using wave dispersion measurements is usually performed using a two-step approach, where the construction of 2-D maps of phase/group velocities at series of frequencies is followed by a point-wise inversion of dispersion data for 1-D depth profiles at each grid point (Bodin & Sambridge, 2009). This approach assumes smoothly varying medium and may suffer from lateral discontinuity; furthermore the minor waveform changes in the monitoring data may be difficult to track from dispersion. On the other hand, we build the baseline shear-wave velocity model from surface waves using wave-equation dispersion inversion followed by FWI to further improve the accuracy and resolution, and finally DD-WI of arrival time shifts for time-lapse images. The models are updated based on the adjoint-state method with a numerical solution of the full elastic-wave equation for arbitrarily complicated medium. In contrast with the two-step method, the inversions we used are able to provide velocity models in the horizontal and depth domain from surface waves in one step with a few iterations. The inversion is sensitive to subtle subsurface property changes by comparing the waveforms directly using the full physics.

In this study we limit the maximum offset to be 3 km. It is straightforward to include CC functions from larger offsets for monitoring subsurface property change at the greater depths, but likely with a lower temporal resolution because of longer recording time of ambient noise for the CC function convergence. Body waves have been observed in the auto- and cross-correlation functions of seismic ambient noise (Roux et al., 2005; Nakata et al., 2016; Saygin et al., 2017). As we use DD measurements of arrival times rather than wave dispersion, the proposed method can be applied for monitoring using body waves (Brenguier et al., 2020). While we apply the method per survey line, the method is ready for estimating subsurface velocity change models in 3-D (the horizontal plane and depth) using 3-D elastic-wave equations, provided that the 3-D seismic responses can be accurately reconstructed from ambient noise. The time-lapse inversion method is easy to implement with existing FWI source codes by simply changing the adjoint source for backward wavefield propagation. Time-lapse inversion using DD measurements of arrival times can also be implemented using ray-tracing, however elastic-wave equation describes the complete wave phenomena without the high-frequency approximation.

The extracted seismic responses contain two parts: the direct (ballistic) waves and the coda part (Shapiro and Campillo, 2004). We apply the method to the ballistic part of the Scholte waves. The coda part can be more sensitive to subtle velocity changes because the multiple scattering process caused by heterogeneities samples the propagation medium very densely and for a long time (Sens-Schönfelder and Wegler, 2006) and has been widely used for detecting very small velocity changes with a spatially uniform change asumption (Hillers et al., 2014). However its convergence requires longer recording time and the sophisticated propagation paths make inversion difficult. Apart from localizing the velocity changes from ballistic surface wave arrivals (de Ridder et al., 2014; Mordret et al., 2014, 2020), there have been studies for determining the spatial extent of changes from coda waves using sensitivity kernels (Obermann et al., 2013), which is derived based on the diffusion approximation (Pacheco & Snieder, 2005) and is more of a modeling perspective. The resolution is lower than that from the wave-equation based inversion.

The observed changes of shear-wave velocity decrease with increasing depths, generally follows the seafloor bathymetry and seems to have a 24-hour cycling pattern. Previous studies (e.g., Takano et al., 2014) have related onshore crustal velocity changes of 0.1-0.3% to the solid earth tide from the gravitational field of the Sun and Moon, which could cause the opening/closure of cracks or pores in the shallow subsurface leading to velocity decrease/increase respectively. The periodicity of non-volcanic tremor at the subduction zone (Nakata et al., 2008) and the microseismicity at the Mid-Atlantic Ridge (Leptokaropoulos et al., 2021) can also be induced by the earth tide. The changes in sea height caused by the ocean tide through the influence of gravity can create overburden loading variations on the seafloor and cause temporal velocity changes (Dean et al., 1994). The velocity changes caused by earth tide decrease with depths (Hillers et al., 2015), consistent with what we have observed. In addition to the solid earth and ocean tides, the pressure loading of long-wavelength ocean infragravity waves can also induce seafloor vertical deformation (seafloor compliance), which is sensitive to the shear modulus structure (Crawford et al., 1999) and therefore could cause shear-wave velocity temporal changes. The physical mechanism behind the sinusoidal temporal velocity changes (up to 1%) in the shallow seafloor observed at this site remain under investigation.

5 Conclusions

In this study, we demonstrate that the new passive monitoring technique provides a cost-effective and environmentally-friendly solution for real-time 4-D quantitative monitoring of subsurface property changes with high temporal (hourly) and spatial (hundreds of meters) resolution. Using seismic ambient noise data recorded by a dense array of OBNs offshore Western Australia, we detect temporal variations of shear-wave velocity up to 1% in the seafloor, with a likely 24-hour cycling pattern. To localize the velocity changes in the subsurface, we first build a high-resolution baseline seafloor model from FWI of Scholte waves. Then from DD-WI of wave arrival time differences we obtain the quantitative time-lapse seafloor images containing the heterogeneous relative velocity variations in the horizontal and depth domain, where the velocity changes decrease with increasing depths. The elastic-wave equation based workflow from building high-resolution baseline model to time-lapse inversion using surface wave measurements honors the full wave physics, is robust to data noise and errors from the baseline model, and is sensitive to subtle velocity changes, which can be applied to dense passive seismic data from seismic arrays and Distributed Acoustic Sensing (DAS) for real-time monitoring of groundwater level, volcano, subduction zone and CO_2 capture storage, in the aim for an in-depth understanding of the evolving 4-D Earth.

Acknowledgments

This research was funded by the Deep Earth Imaging Future Science Platform, CSIRO. This work was supported by resources provided by the Pawsey Supercomputing Centre with funding from the Australian Government and the Government of Western Australia. The raw seismic data of the Gorgon Ocean Bottom Node Seismic Survey (ID: ENO0603054) can be requested from the National Offshore Petroleum Information Management System (NOPIMS) via contacting AusGeoData@ga.gov.au. We thank Chevron Australia for their assistance with the data. We thank Dr. Yuqing Chen for providing the starting model of shear-wave velocity for baseline FWI.

Open Research

The data used for reproducing the figures, including the hourly CC functions, dv/v measurements and seismic velocity models, are publicly available at https://doi.org/10.5281/zenodo.6804990.

References

Bodin, T., & Sambridge, M. (2009). Seismic tomography with the reversible jump algorithm. Geophysical Journal International, 178(3), 1411-1436.

Brenguier, F., Shapiro, N. M., Campillo, M., Ferrazzini, V., Duputel, Z., Coutant, O., & Nercessian, A. (2008). Towards forecasting volcanic eruptions using seismic noise. Nature Geoscience, 1(2), 126-130.

Brenguier, F., Rivet, D., Obermann, A., Nakata, N., Boué, P., Lecocq, T., ... & Shapiro, N. (2016). 4-D noise-based seismology at volcanoes: Ongoing efforts and perspectives. Journal of Volcanology and Geothermal Research, 321, 182-195.

Brenguier, F., Courbis, R., Mordret, A., Campman, X., Boué, P., Chmiel, M., ... & Hollis, D. (2020). Noise-based ballistic wave passive seismic monitoring. Part 1: body waves. Geophysical Journal International, 221(1), 683-691.

Chen, Y. and Saygin, E. (2022). 3-D S Wave Imaging via Robust Neural Network Interpolation of 2-D Profiles from Wave equation Dispersion Inversion of Seismic, J. Geophys. Res.-Solid Earth, in-review. https://www.essoar.org/doi/abs/10.1002/essoar.10511223.1

Crawford, W. C., Webb, S. C., & Hildebrand, J. A. (1999). Constraints on melt in the lower crust and Moho at the East Pacific Rise, 9 48′ N, using seafloor compliance measurements. Journal of Geophysical Research: Solid Earth, 104(B2), 2923-2939.

Dean, G., Hardy, R., & Eltvik, P. (1994). Monitoring compaction and compressibility changes in offshore chalk reservoirs. SPE Formation Evaluation, 9(01), 73-76.

Denli, H., & Huang, L. (2009). Double-difference elastic waveform tomography in the time domain. In SEG Technical Program Expanded Abstracts 2009 (pp. 2302-2306). Society of Exploration Geophysicists.

De Ridder, S. A. L., & Biondi, B. L. (2013). Daily reservoir-scale subsurface monitoring using ambient seismic noise. Geophysical Research Letters, 40(12), 2969-2974.

De Ridder, S. A. L., Biondi, B. L., & Clapp, R. G. (2014). Time-lapse seismic noise correlation tomography at Valhall. Geophysical Research Letters, 41(17), 6116-6122.

Fichtner, A., Bunge, H. P., & Igel, H. (2006). The adjoint method in seismology: I. Theory. Physics of the Earth and Planetary Interiors, 157(1-2), 86-104.

Guo, P., Singh, S.C., Vaddineni, V.A. et al. (2022). Lower oceanic crust formed by in situ melt crystallization revealed by seismic layering. Nature Geoscience, https://doi.org/10.1038/s41561-022-00963-w

Hicks, E., Hoeber, H., Houbiers, M., Lescoffit, S. P., Ratcliffe, A., & Vinje, V. (2016). Time-lapse full-waveform inversion as a reservoir-monitoring tool—A North Sea case study. The Leading Edge, 35(10), 850-858.

Hillers, G., Retailleau, L., Campillo, M., Inbal, A., Ampuero, J. P., & Nishimura, T. (2015). In situ observations of velocity changes in response to tidal deformation from analysis of the high-frequency ambient wavefield. Journal of Geophysical Research: Solid Earth, 120(1), 210-225.

Kamei, R. and D. Lumley (2017). Full waveform inversion of repeating seismic events to estimate time-lapse velocity changes. Geophysical Journal International 209(2), 1239–1264.

Leptokaropoulos, K., Harmon, N., Hicks, S. P., Rychert, C. A., Schlaphorst, D., & Kendall, J. M. (2021). Tidal triggering of microseismicity at the Equatorial Mid-Atlantic Ridge, Inferred from the PI-LAB experiment. Journal of Geophysical Research: Solid Earth, 126(9), e2021JB022251.

Li, J., Feng, Z., & Schuster, G. (2017). Wave-equation dispersion inversion. Geophysical Journal International, 208(3), 1567-1578.

Lumley, D. E. (2001). Time-lapse seismic reservoir monitoring. Geophysics, 66(1), 50-53.

Mao, S., M. Campillo, R. D. van der Hilst, et al. (2019). High temporal resolution monitoring of small variations in crustal strain by dense seismic arrays. Geophysical Research Letters 46(1), 128–137.

Mordret, A., Courbis, R., Brenguier, F., Chmiel, M., Garambois, S., Mao, S., ... & Hollis, D. (2020). Noise-based ballistic wave passive seismic monitoring–Part 2: surface waves. Geophysical Journal International, 221(1), 692-705.

Mordret, A., N. M. Shapiro, and S. Singh (2014). Seismic noise-based time-lapse monitoring of the valhall overburden. Geophysical Research Letters 41(14), 4945–4952.

Nakata, N., Boué, P., Brenguier, F., Roux, P., Ferrazzini, V., & Campillo, M. (2016). Body and surface wave reconstruction from seismic noise correlations between arrays at Piton de la Fournaise volcano. Geophysical Research Letters, 43(3), 1047-1054.

Nakata, R., Suda, N., & Tsuruoka, H. (2008). Non-volcanic tremor resulting from the combined effect of Earth tides and slow slip events. Nature Geoscience, 1(10), 676-678.

Obermann, A., Planès, T., Larose, E., Sens-Schönfelder, C., & Campillo, M. (2013). Depth sensitivity of seismic coda waves to velocity perturbations in an elastic heterogeneous medium. Geophysical Journal International, 194(1), 372-382.

Pacheco, C., & Snieder, R. (2005). Time-lapse travel time change of multiply scattered acoustic waves. The Journal of the Acoustical Society of America, 118(3), 1300-1310.

Richter, T., Sens-Schönfelder, C., Kind, R., & Asch, G. (2014). Comprehensive observation and modeling of earthquake and temperature-related seismic velocity changes in northern Chile with passive image interferometry. Journal of Geophysical Research: Solid Earth, 119(6), 4747-4765.

Roche, B., Bull, J. M., Marin-Moreno, H., Leighton, T. G., Falcon-Suarez, I. H., Tholen, M., ... & Faggetter, M. (2021). Time-lapse imaging of CO_2 migration within near-surface sediments during a controlled sub-seabed release experiment. International Journal of Greenhouse Gas Control, 109, 103363.

Rodríguez Tribaldos, V., & Ajo-Franklin, J. B. (2021). Aquifer monitoring using ambient seismic noise recorded with distributed acoustic sensing (DAS) deployed on dark fiber. Journal of Geophysical Research: Solid Earth, 126(4), e2020JB021004.

Roux, P., Sabra, K. G., Gerstoft, P., Kuperman, W. A., & Fehler, M. C. (2005). P-waves from cross-correlation of seismic noise. Geophysical Research Letters, 32(19).

Saygin, E., Cummins, P. R., & Lumley, D. (2017). Retrieval of the P wave reflectivity response from autocorrelation of seismic noise: Jakarta Basin, Indonesia. Geophysical Research Letters, 44(2), 792-799.

Schimmel, M., Stutzmann, E., & Gallart, J. (2011). Using instantaneous phase coherence for signal extraction from ambient noise data at a local to a global scale. Geophysical Journal International, 184(1), 494-506.

Sens-Schönfelder, C. and U. Wegler (2006). Passive image interferometry and seasonal variations of seismic velocities at Merapi volcano, Indonesia. Geophysical Research Letters 33 (21), L21302.

Shapiro, N. M. and M. Campillo (2004). Emergence of broadband rayleigh waves from correlations of the ambient seismic noise. Geophysical Research Letters 31(7).

Shen, X. (2010). Near-surface velocity estimation by weighted early-arrival waveform inversion. In SEG Technical Program Expanded Abstracts 2010 (pp. 1975-1979). Society of Exploration Geophysicists.

Shipp, R. M., & Singh, S. C. (2002). Two-dimensional full wavefield inversion of wide-aperture marine seismic streamer data. Geophysical Journal International, 151(2), 325-344.

Stehly, L., Campillo, M., & Shapiro, N. M. (2006). A study of the seismic noise from its long-range correlation properties. Journal of Geophysical Research: Solid Earth, 111(B10).

Takano, T., Brenguier, F., Campillo, M., Peltier, A., & Nishimura, T. (2020). Noise-based passive ballistic wave seismic monitoring on an active volcano. Geophysical Journal International, 220(1), 501-507.

Takano, T., Nishimura, T., Nakahara, H., Ohta, Y., & Tanaka, S. (2014). Seismic velocity changes caused by the Earth tide: Ambient noise correlation analyses of small-array data. Geophysical Research Letters, 41(17), 6131-6136.

Tarantola, A. (1984). Inversion of seismic reflection data in the acoustic approximation. Geophysics. 49, 1259-1266.

Virieux, J. (1986). P-SV wave propagation in heterogeneous media: Velocity-stress finite-difference method. Geophysics, 51(4), 889-901.

Yang, D., Liu, F., Morton, S., Malcolm, A., & Fehler, M. (2016). Time-lapse full-waveform inversion with ocean-bottom-cable data: Application on Valhall field. Geophysics, 81(4), R225-R235.

Yuan, Y. O., Simons, F. J., & Tromp, J. (2016). Double-difference adjoint seismic tomography. Geophysical Journal International, 206(3), 1599-1618.

Zhang, Z., & Huang, L. (2013). Double-difference elastic-waveform inversion with prior information for time-lapse monitoring. Geophysics, 78(6), R259-R273.

AGU PUBLICATIONS

Geophysical Research Letters

Supporting Information for

Towards Hourly 4-D Subsurface Monitoring using Seismic Ambient Noise

Peng Guo[1,*] and Erdinc Saygin[1,2]

1. Deep Earth Imaging Future Science Platform, The Commonwealth Scientific and Industrial Research Organisation (CSIRO), Kensington 6151, WA, Australia.

2. Department of Physics, School of Physics, Mathematics and Computing, Faculty of Engineering and Mathematical Sciences, University of Western Australia, Crawley 6009, WA, Australia.

Corresponding author: Peng Guo (peng.guo@csiro.au)

Contents of this file

Text S1 – S2

Figures S1 to S16

Please note that, figures related to the Gorgon OBN survey are from Line 3924, unless otherwise stated.

Text S1.

Misfit function and adjoint source for trace-normalized FWI

The misfit function $\boldsymbol{J}$ for the trace-normalized FWI is defined as (Shen, 2010)

$$J = \sum_{i=1}^{Ns} \sum_{j=1}^{Nr} \left\| \frac{\mathrm{s}_{i,j}}{\|\mathrm{s}_{i,j}\|} - \frac{\mathrm{d}_{i,j}}{\|\mathrm{d}_{i,j}\|} \right\|^2 \quad \text{(S1)},$$

where $\boldsymbol{s_{i,j}}$ and $\boldsymbol{d_{i,j}}$ are seismic traces (1-D time-series vectors) from the synthetic and field data, respectively, i and j are the indexes for the sources and receivers, Ns and Nr are the number of sources and receivers, and $\| \quad \|$ is the l-2 norm operator.

Considering that $\frac{\partial \|\mathrm{s}_{i,j}\|}{\partial \mathrm{s}_{i,j}} = \frac{\mathrm{s}_{i,j}}{\|\mathrm{s}_{i,j}\|}$, the adjoint source is

$$\chi_{i,j} = \frac{\partial J}{\partial s_{i,j}} = \left(\frac{\mathrm{s}_{i,j}}{\|\mathrm{s}_{i,j}\|} - \frac{\mathrm{d}_{i,j}}{\|\mathrm{d}_{i,j}\|} \right) \left(\frac{\|\mathrm{s}_{i,j}\| - \frac{\mathrm{s}_{i,j}}{\|\mathrm{s}_{i,j}\|} \mathrm{s}_{i,j}}{\|\mathrm{s}_{i,j}\|^2} \right) \quad \text{(S2)}$$

Text S2.

Synthetic tests: sensitivity of time-lapse inversion to baseline model errors and data noise.

The observed temporal velocity changes (up to ~1%) is subtle, therefore it is important to test if these velocity changes are real, not coming from the unfitted data in the baseline inversion. We perform a series of synthetic tests. We use the same frequency range, recording geometry and inversion parameters of the field data for these tests. We use the FWI derived model (Fig. 4a) as the baseline model for generating the 'observed' baseline data. We then add 1% positive and negative Gaussian-shaped velocity anomalies ('temporal changes', 1 km horizontal extension and 0.2 km thickness, Fig. S11a) to the baseline model (Fig. 4a) for generating the 'observed' monitoring data. We first use the true baseline model (Fig. 4a) as the starting model for DD-WI as a benchmark, with the inverted models of velocity changes in Fig. S11b and S11c from DD-WI using waveform and travel time differences respectively.

The tomographic velocity model in Fig. S3a, which contains much larger difference with the true baseline model than the added velocity anomalies, is then used as the starting model for the DD-WI. By using the tomographic model as the baseline model, we create a scenario similar to the field data study where the differences between the baseline model used for inversion and the ground truth baseline model are very likely much larger than the observed temporal changes, and we are able to test the robustness of time-lapse inversion to baseline models. Both the DD-WI methods using waveform (Yang et al., 2016) and travel time differences have been applied. The results suggest that the proposed algorithm is able to recover the subtle velocity differences very well (Fig. S12c), and is less sensitive to the baseline model than DD-WI using waveform differences (Fig. S12b). We then add noise to the baseline and monitoring data respectively. The signal to noise ratio (S/N) is ~8, lower than that of the extracted hourly CC functions, and the inverted models (Fig. S13) suggest that DD-WI using travel times is more robust to noise. Fig. S14 suggests that the method is able to recover more subtle velocity perturbations (0.5%).

We also test if the inversion methods and data settings can recover velocity anomalies of smaller size (0.5 km horizontal extension and 0.2 km thickness, Fig. S15a). When using the true baseline model (Fig. 4a) as the starting model for time-lapse inversion (which is not going to happen in field data studies, benchmark test), DD-WI using waveform differences can recover the anomalies better (Fig. S15). However, when there are errors in the baseline model, DD-WI using travel time differences provides better results (Fig. S16). Therefore the proposed method is robust to data noise and errors in the baseline model, and the velocity temporal changes localized by DD-WI using travel time differences are reliable.

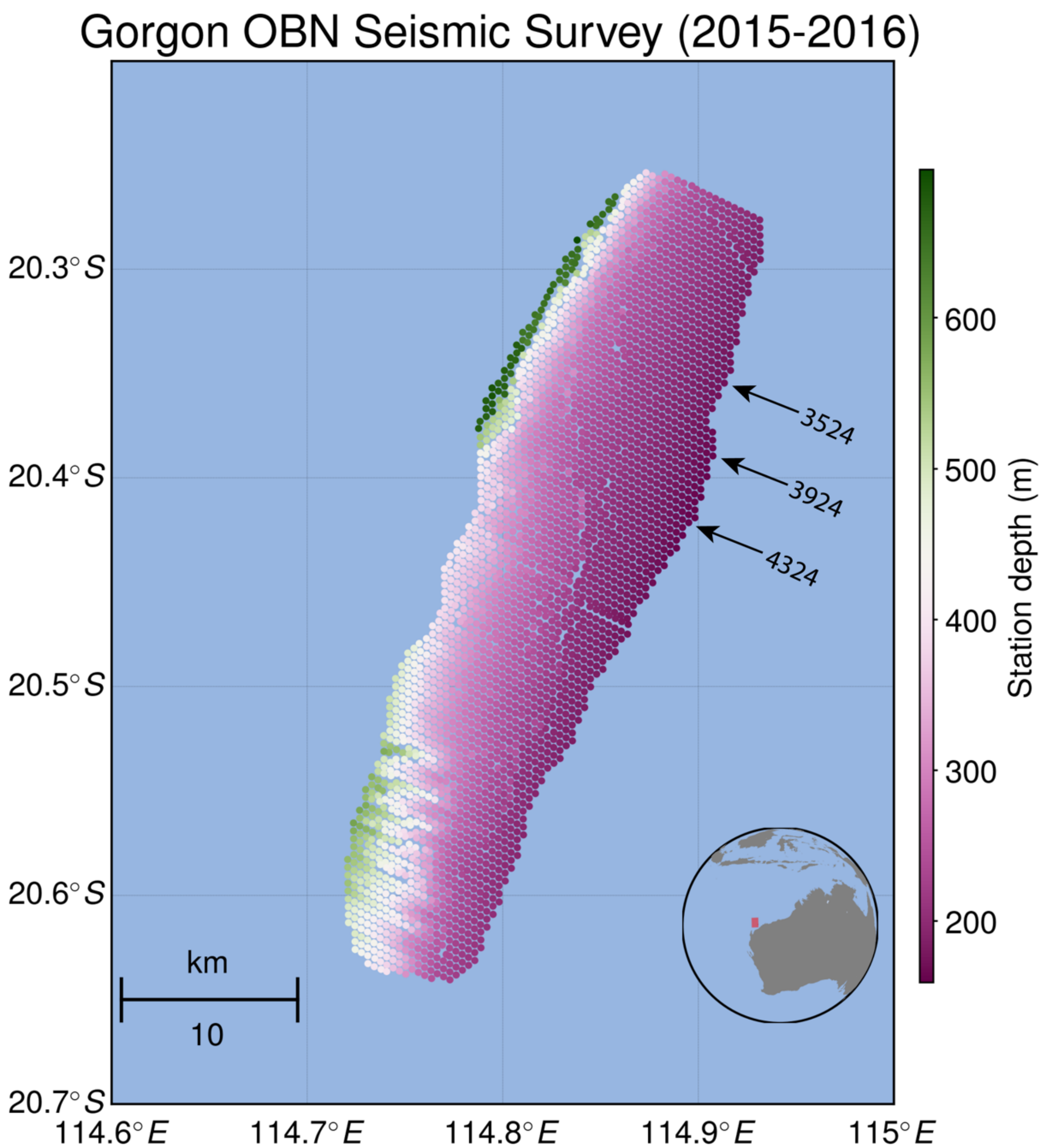

Figure S1. Ocean Bottom Node (OBN) seismic survey in the Gorgon gas field of the offshore of Western Australia by Chevron Australia and its partners. The colors on the OBNs suggest water depths. The black arrows indicate the positions of Line 3524, 3924 and 4324, respectively.

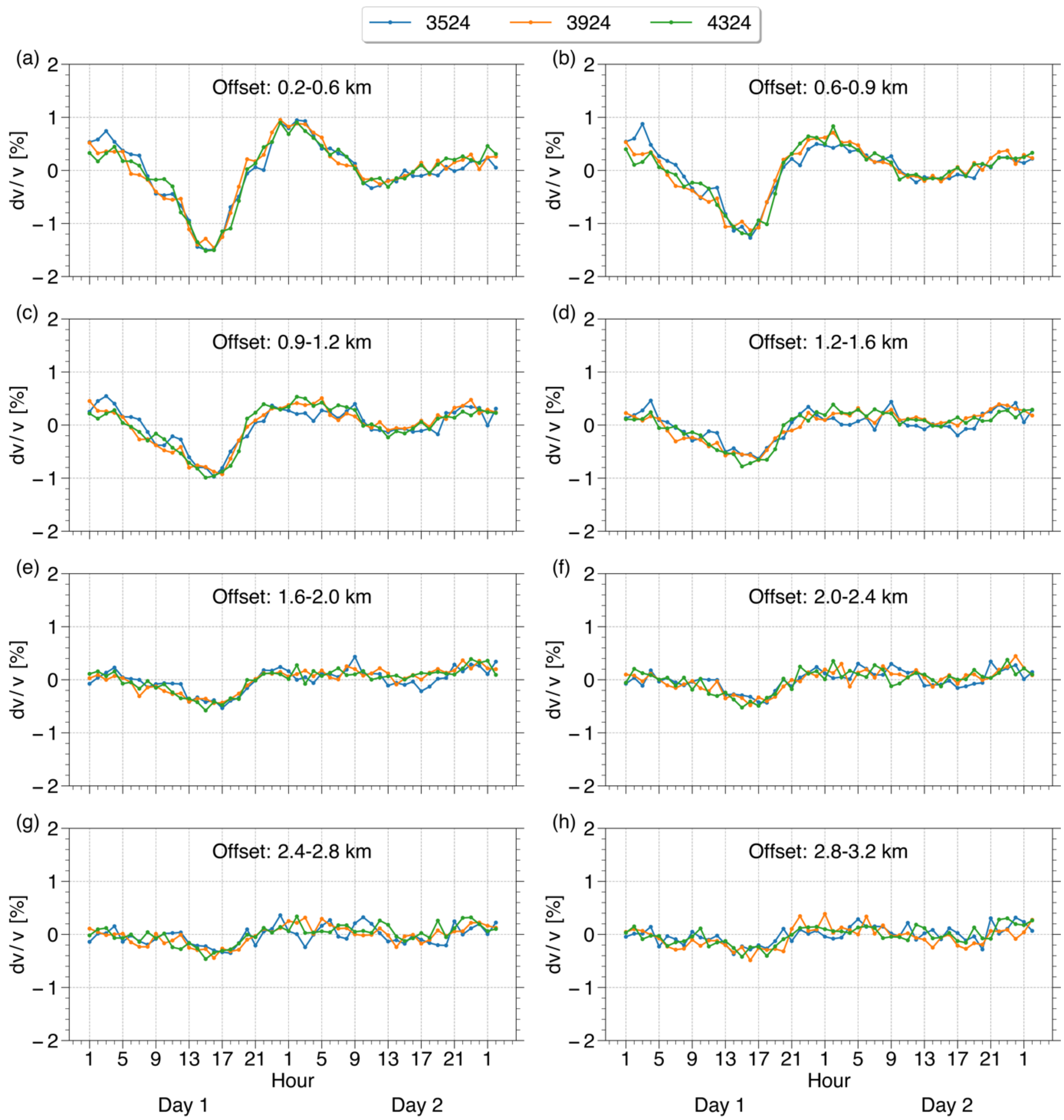

Figure S2. The shear-wave velocity changes (dv/v) of the seafloor at an hourly basis for Day 1 and Day 2 of 2016 from Lines 3524, 3924 and 4324, from CC functions of different offset ranges. The velocity changes were estimated using the stretching method from the ballistic part of the extracted Scholte waves of the CC functions.

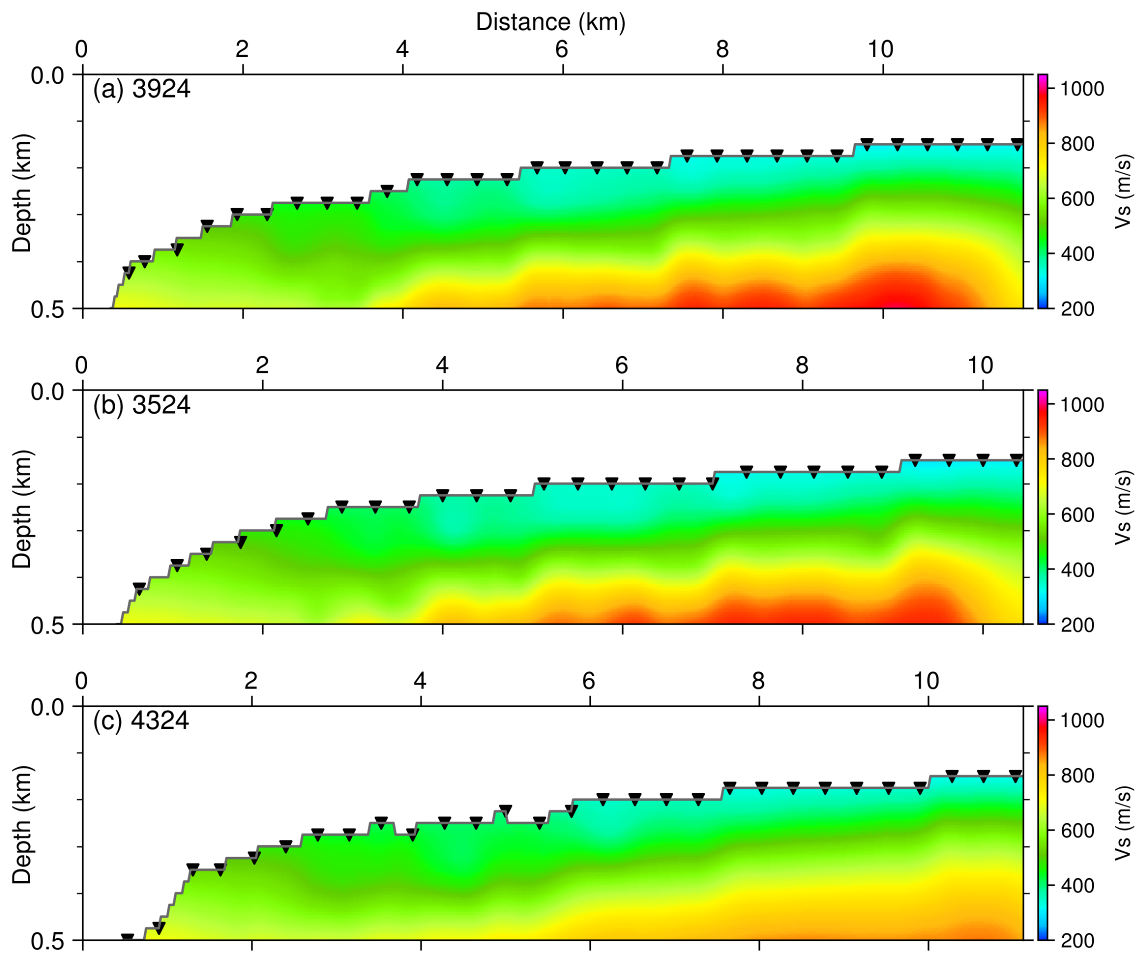

Figure S3. The velocity models from wave-equation dispersion inversion (Chen & Saygin, 2022), which are used as the starting models for baseline FWI. (a), (b) and (c) are the shear-wave velocity models for Line 3924, 3524 and 4324 (Fig. S2), respectively.

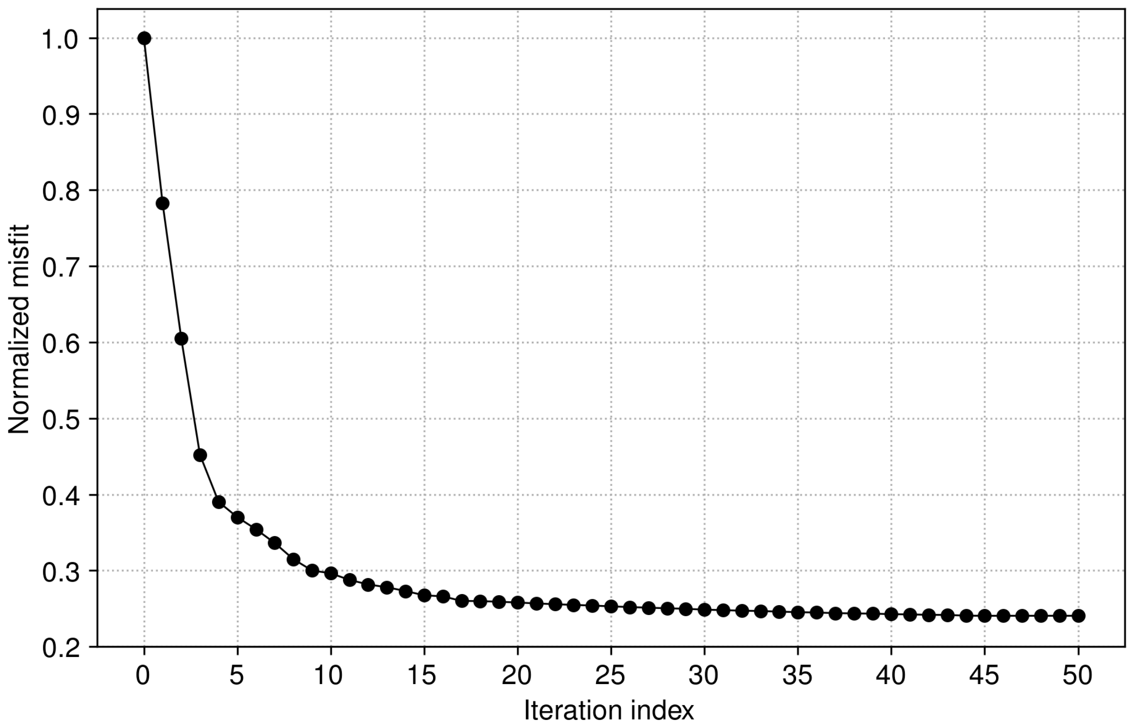

Figure S4. Waveform misfit as a function of iterations for trace-normalized FWI (baseline FWI). The waveform misfit was calculated using equation S1.

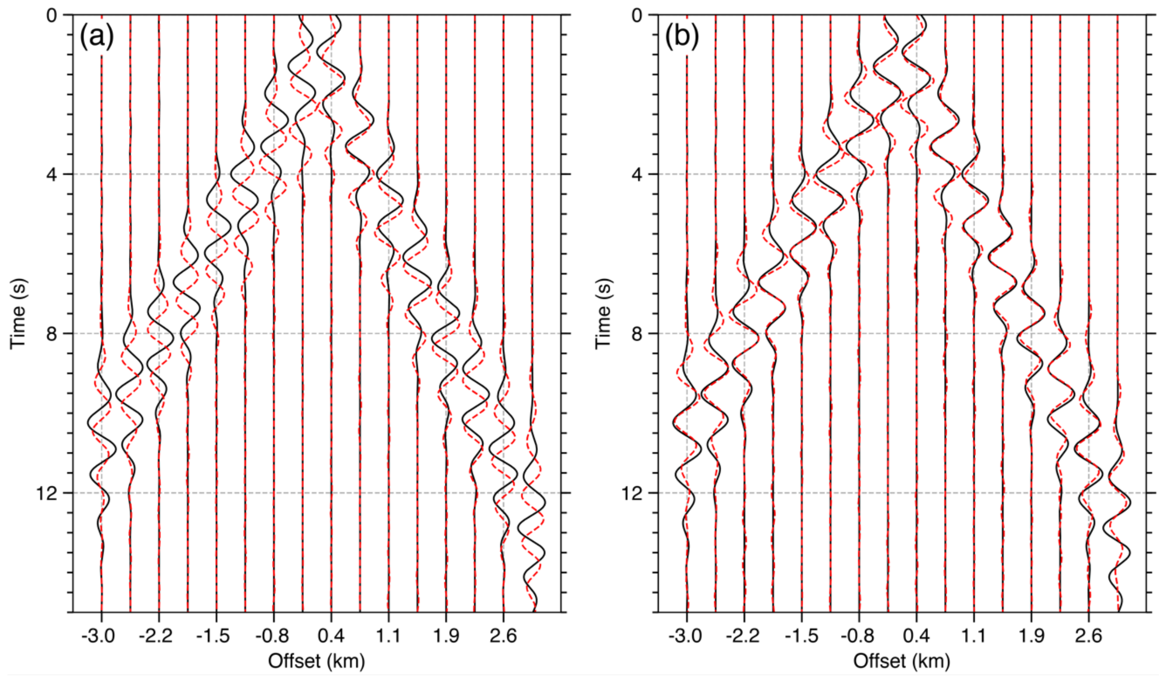

Figure S5. A comparison of observed (extracted from ambient noise) and synthetic seismic waveform data. (a) The observed data (black) and the synthetic waveform (dashed red) using the starting model (Fig. S3a) of baseline FWI, and (b) the observed data (black) and the synthetic waveform (dashed red) using the final model from baseline FWI (Fig. 4a). The waveform match between observed and synthetic data has been much improved after baseline FWI.

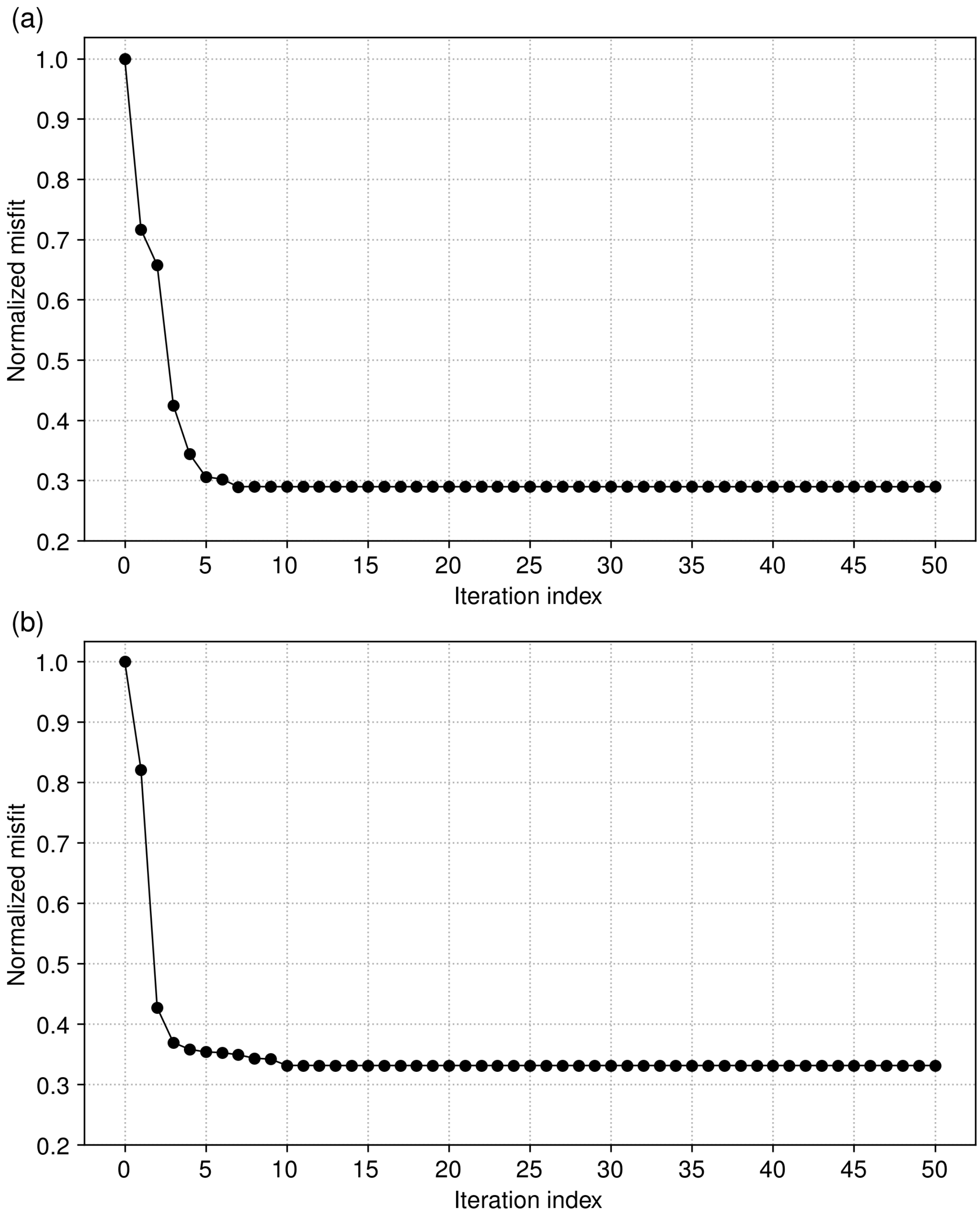

Figure S6. Misfit as a function of iterations for DD-WI, for (a) Hour 15 Day 1 and (b) Hour 1 Day 2. The misfit was calculated using equation 1.

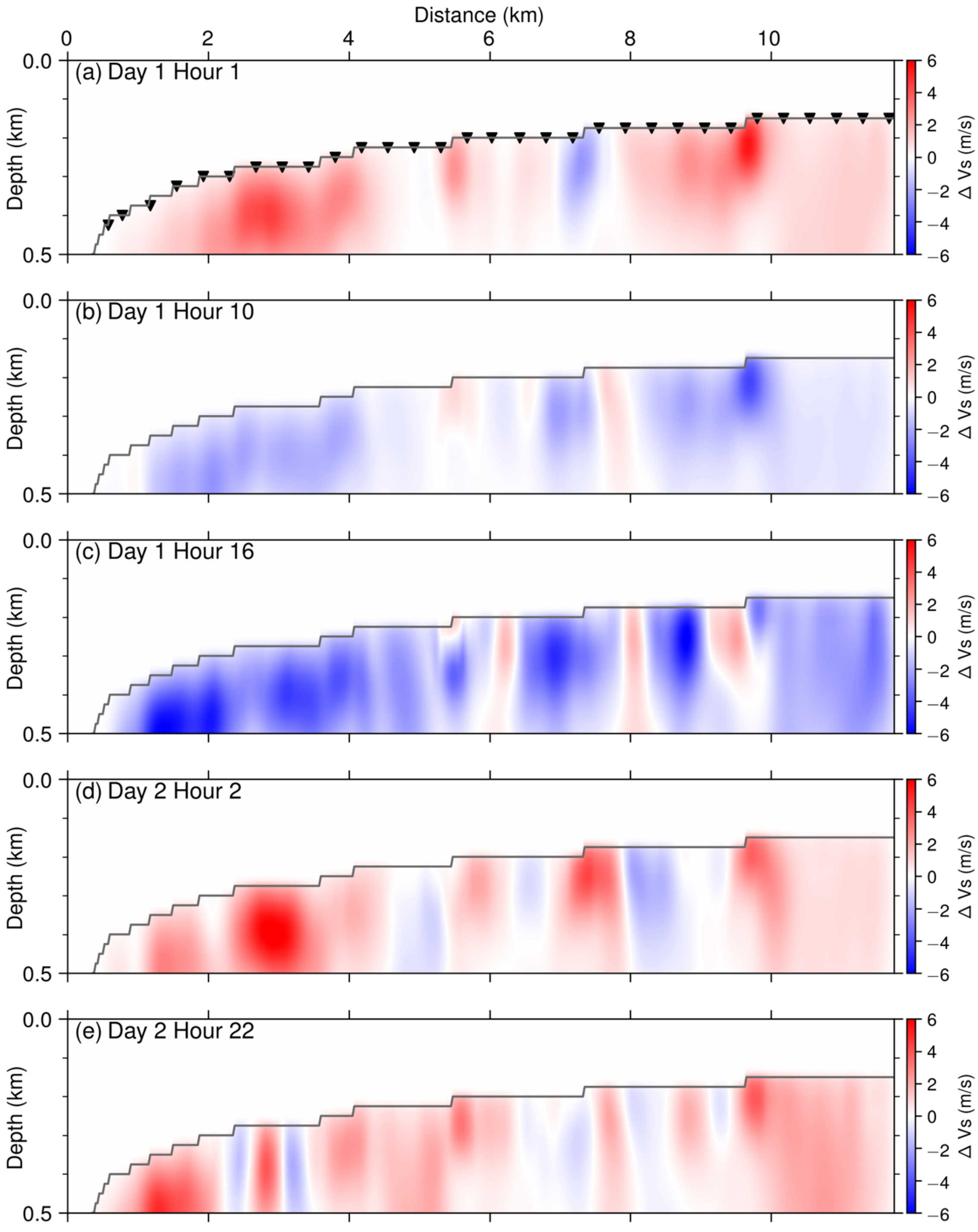

Figure S7. Time-lapse subsurface models of velocity changes from more hours compared with the baseline model (Fig. 4a). The black triangles in (a) indicate the locations of OBNs.

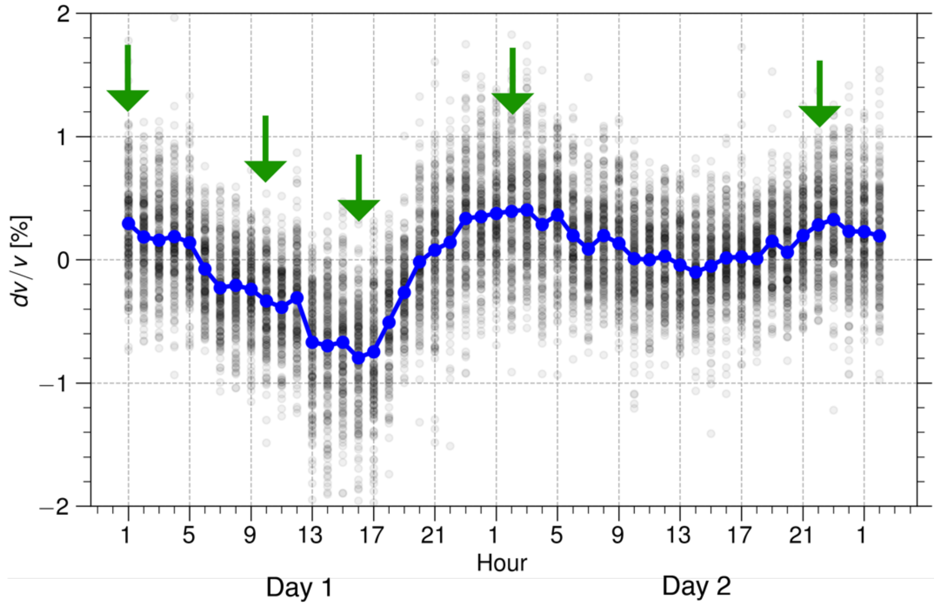

Figure S8. The relative shear-wave velocity changes (dv/v) of the seafloor at an hourly basis for Day 1 and Day 2 of 2016 (the same with Fig. 2a), estimated using the stretch method assuming a spatially homogeneous dv/v. The green arrows from left to right indicate the dv/v for the time-lapse images in Fig. S7 from top to bottom.

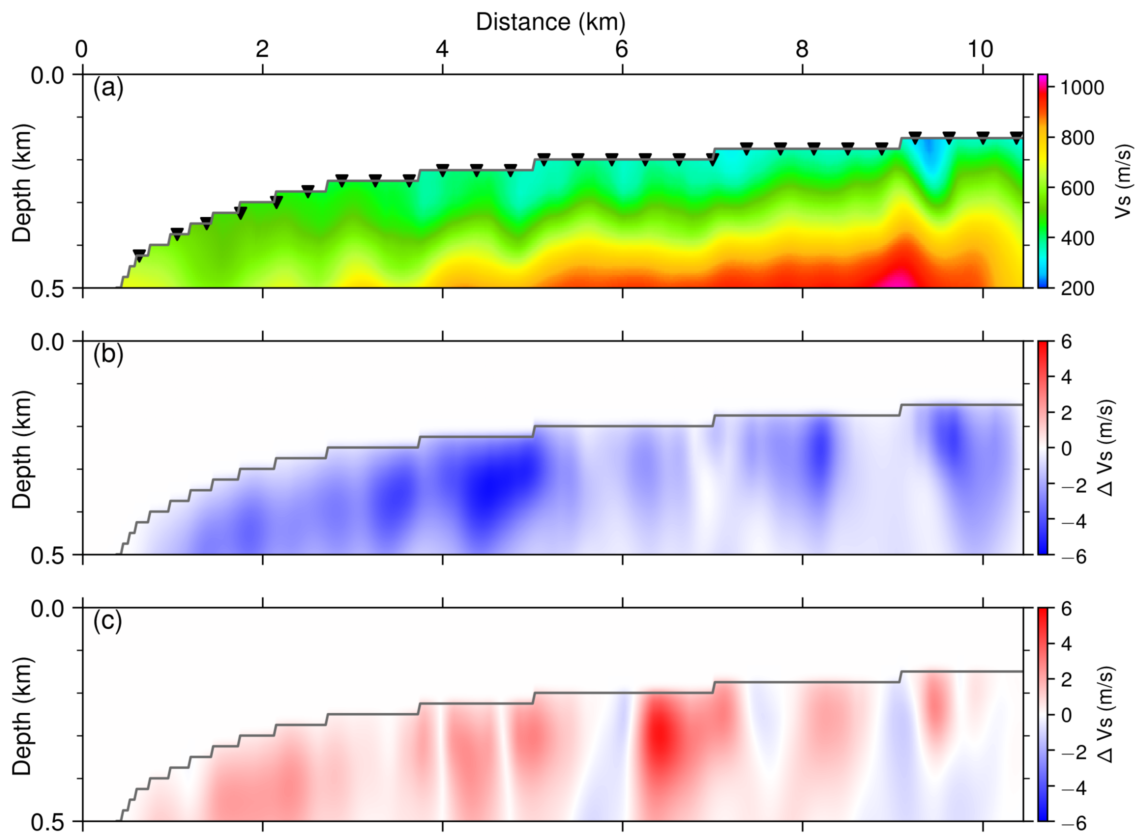

Figure S9. Baseline velocity model and time-lapse subsurface models of velocity changes in the shallow seafloor for Line 3524. The starting model for baseline FWI is Fig. S3b. (a) The high-resolution baseline velocity model from trace-normalized FWI, which is used as the starting model for DD-WI. (b) The time-lapse image of velocity changes for Hour 15 Day 1. (c) The time-lapse image of velocity changes for Hour 1 Day 2. The black triangles in (a) indicate the locations of the OBNs.

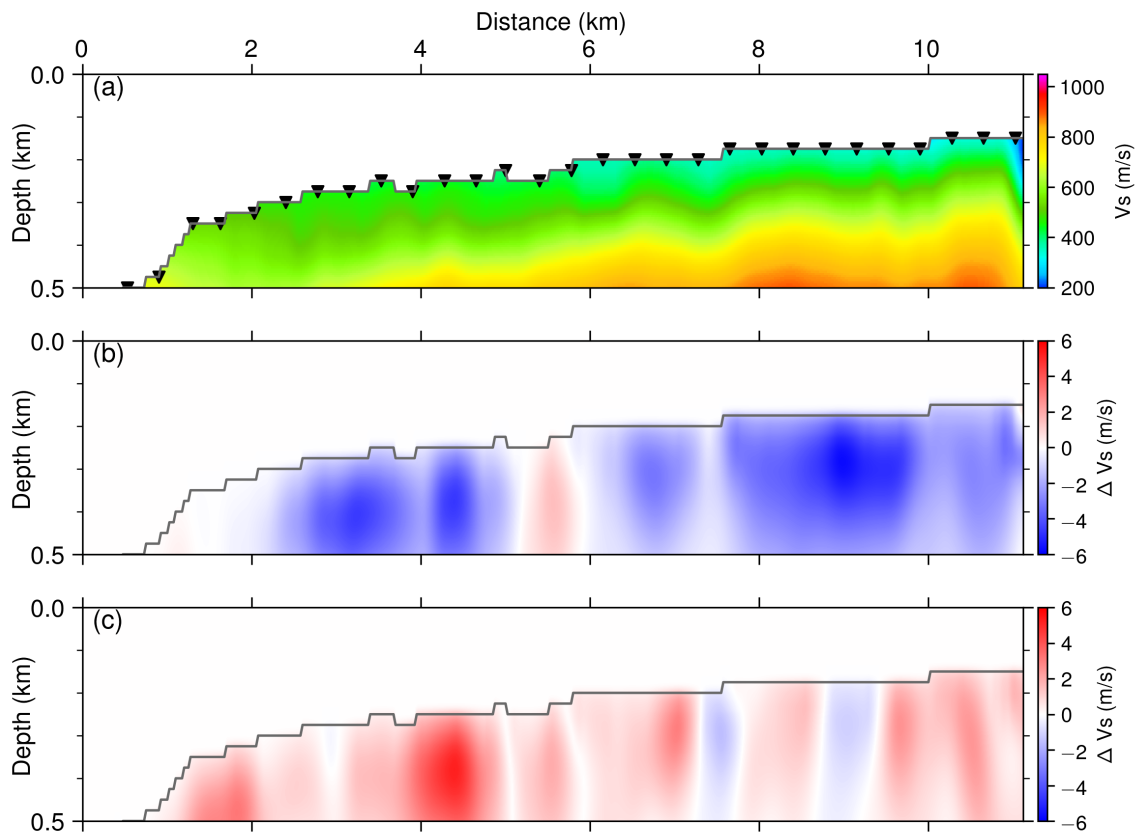

Figure S10. The same with Fig. S9 but for Line 4324 and the starting model for baseline FWI is Fig. S3c.

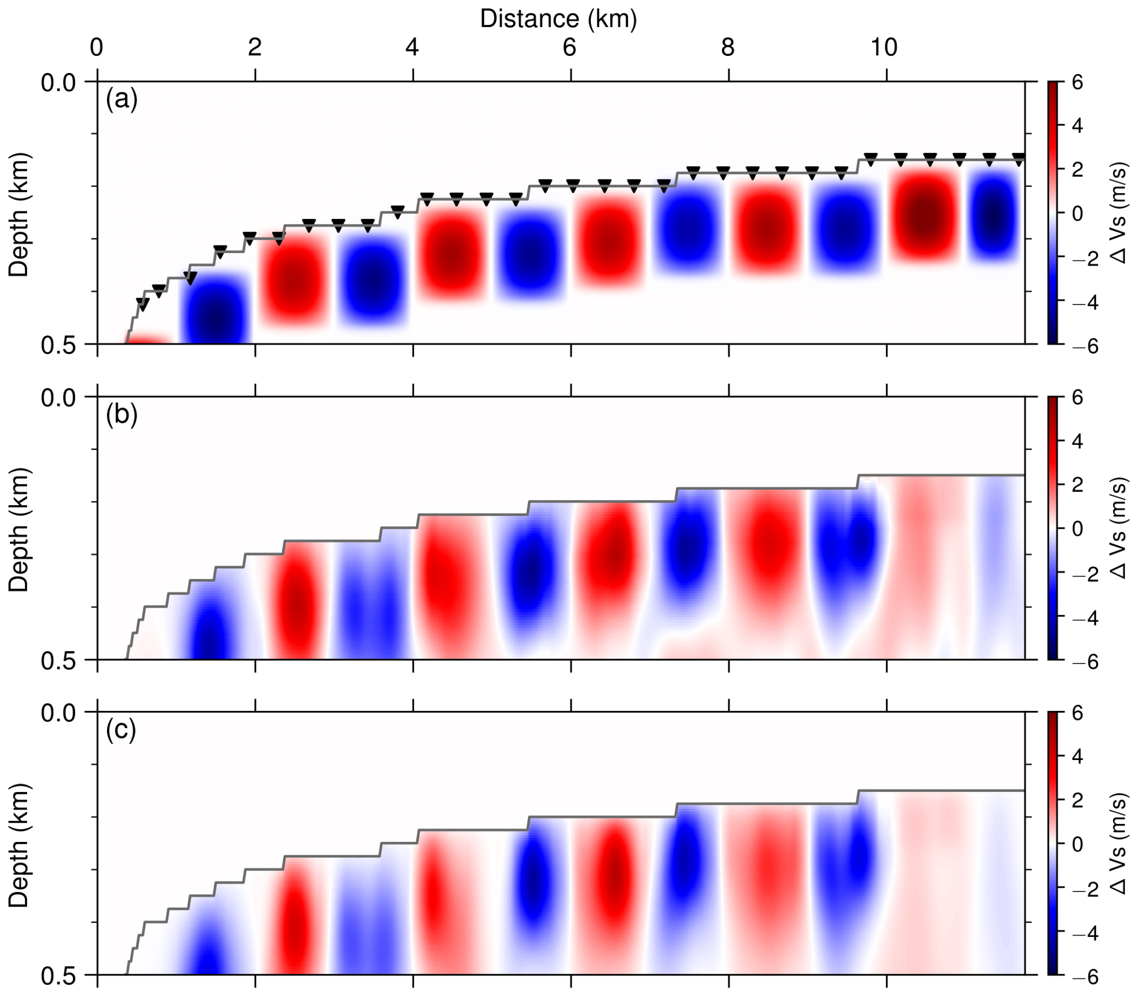

Figure S11. The 'true' time-lapse model was generated by adding 1% positive and negative Gaussian-shape velocity anomalies to the baseline velocity model (Fig. 4a). Each of the anomaly has 1 km lateral extension and 0.2 km thickness. The baseline data was generated using the baseline velocity model (Fig. 4a), and the monitoring data was generated using the 'true' time-lapse model. As a benchmark tests, DD-WI starts from the true baseline model (Fig. 4a) to see how well these perturbations can be recovered. (a) The true velocity anomalies (changes), (b) the inverted velocity anomalies from DD-WI using waveform differences, and (c) the inverted velocity anomalies from DD-WI using arrival time differences. The inverted velocity anomaly model is used as the benchmark for the following tests.

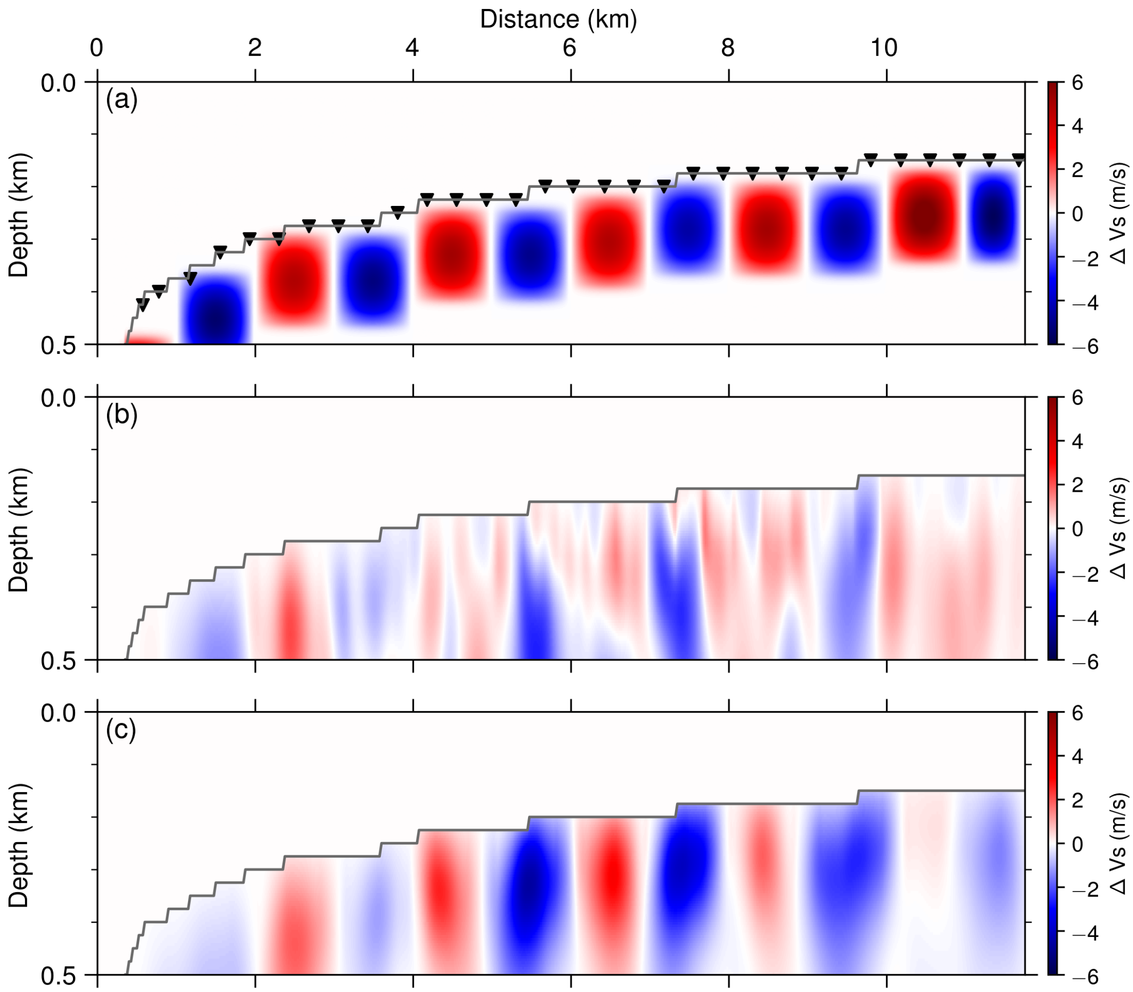

Figure S12. The same with Fig. S11, except that instead of starting DD-WI from the 'true' baseline model (Fig. 4a), we use the model in Fig. S3a as the starting model for DD-WI. The model difference between Fig. S3a and Fig. 4a are much larger than the added velocity anomalies. (a) The true velocity anomalies, (b) the inverted velocity anomalies from DD-WI using waveform differences, and (c) the inverted velocity anomalies from DD-WI using arrival time differences.

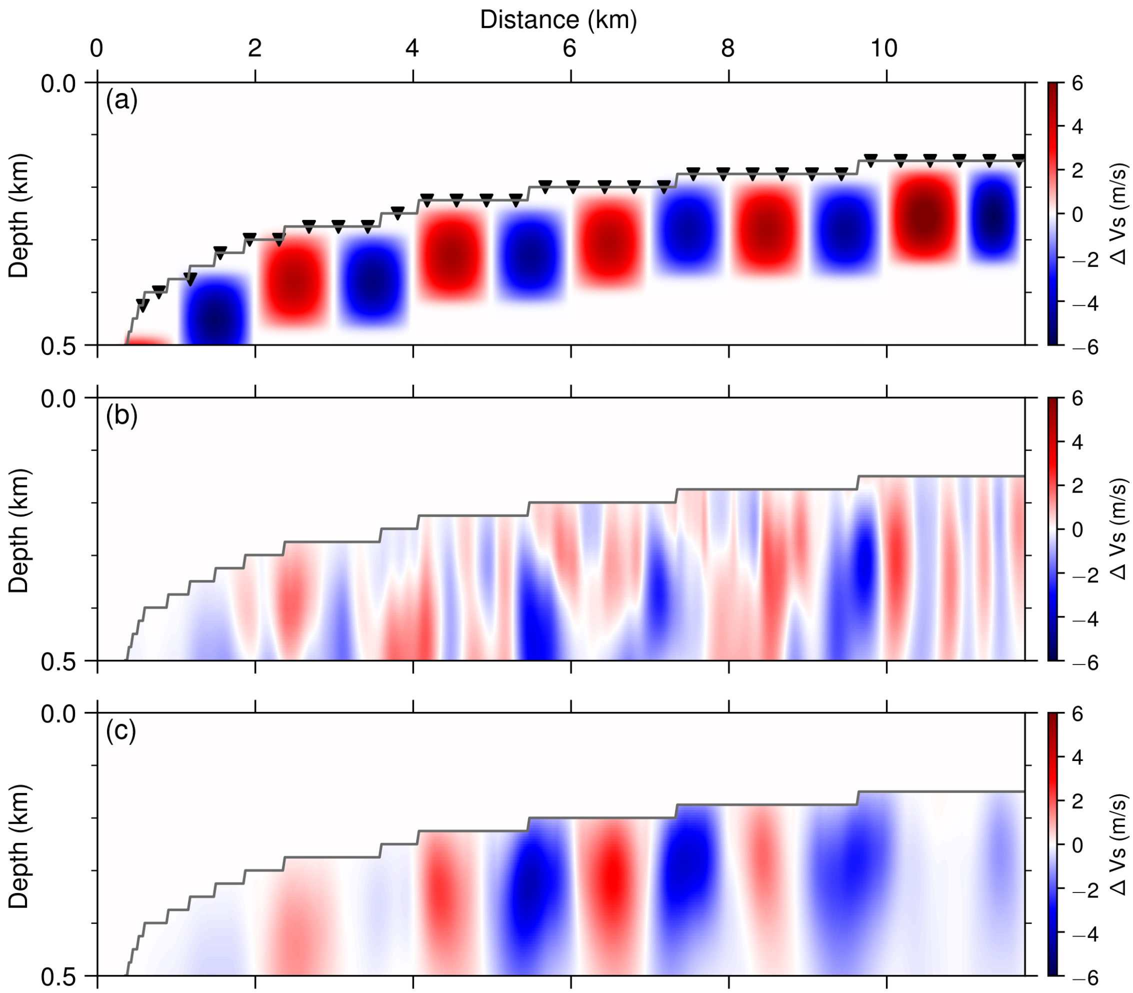

Figure S13. The same with Fig. 12, except that we add noise into the baseline and monitoring data. Signal to noise ratio (S/N) is about 8, lower than that of the extracted CC functions (Fig. 1c) from ambient noise. (a) The true velocity anomalies, (b) the inverted velocity anomalies from DD-WI using waveform differences, and (c) the inverted velocity anomalies from DD-WI using arrival time differences.

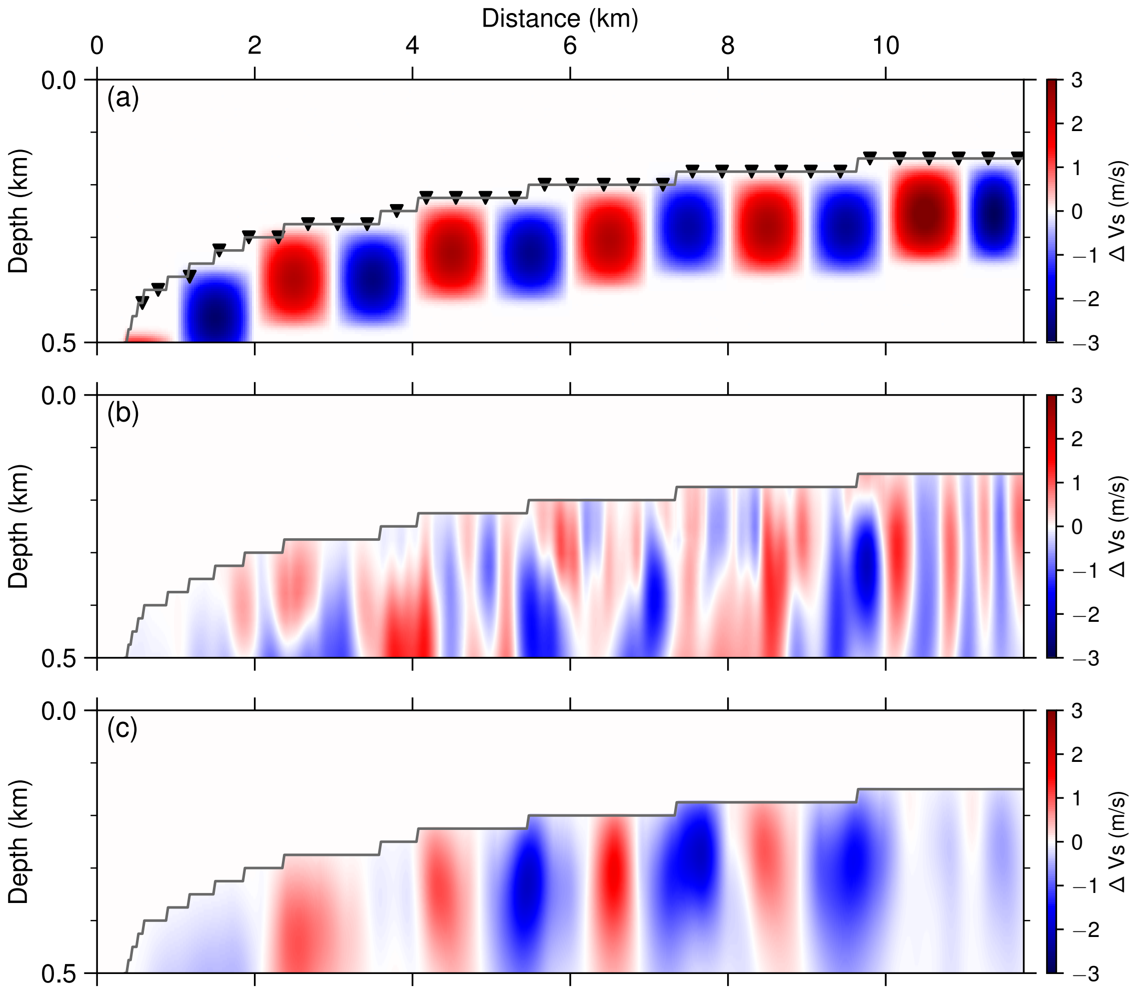

Figure S14. The same with Fig. 13, except that the added velocity anomalies are more subtle, 0.5% of the background velocity. (a) The true velocity anomalies, (b) the inverted velocity anomalies from DD-WI using waveform differences, and (c) the inverted velocity anomalies from DD-WI using arrival time differences.

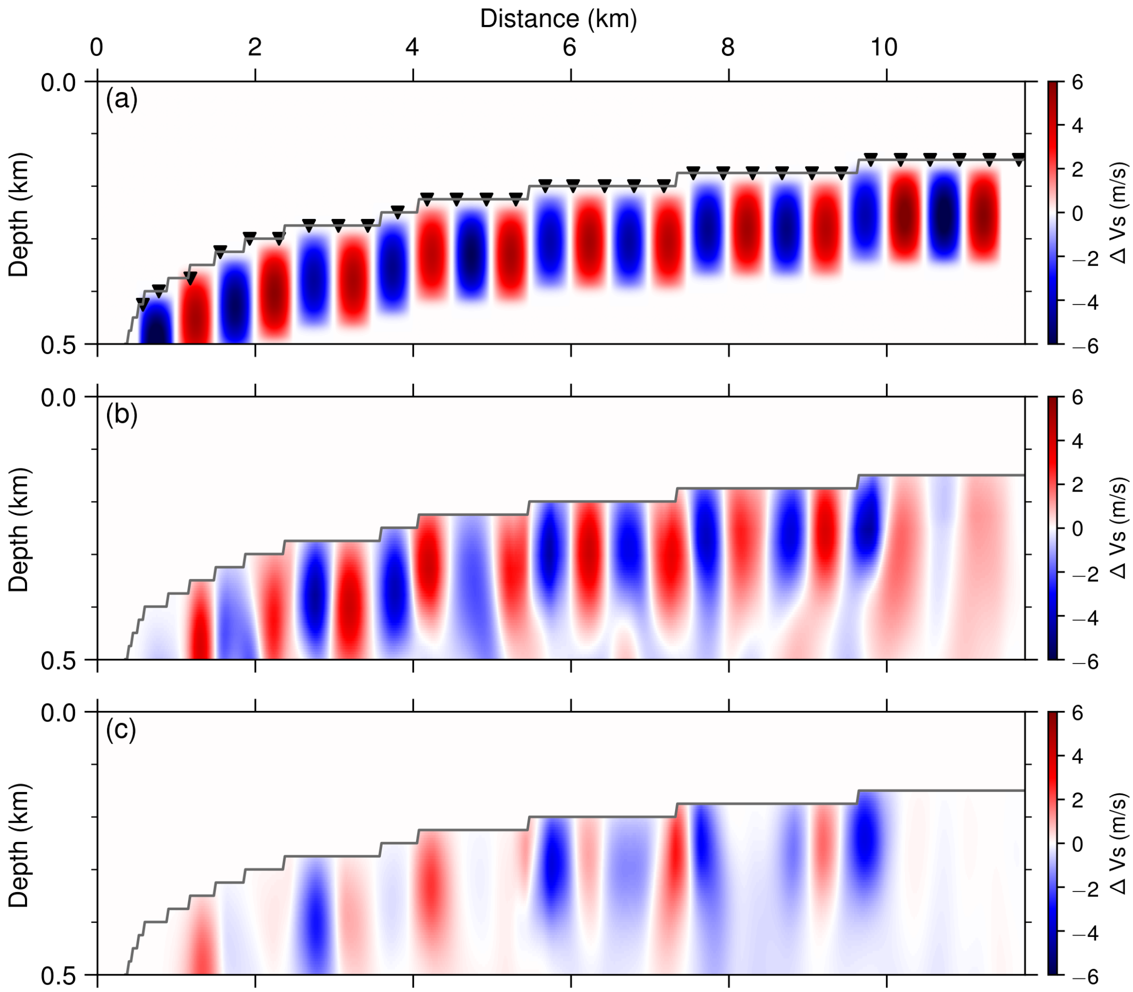

Figure S15. The 'true' time-lapse model was generated by adding 1% positive and negative Gaussian-shape velocity anomalies to the baseline velocity model (Fig. 4a). Each of the anomalies has 0.5 km lateral extension and 0.2 km thickness. The baseline data was generated using the baseline velocity model, and the monitoring data was generated using the 'true' time-lapse model. As a benchmark test, DD-WI starts from the true baseline model (Fig. 4a) to see how well these perturbations can be recovered. (a) The true velocity anomalies, (b) the inverted velocity anomalies from DD-WI using waveform differences, and (c) the inverted velocity anomalies from DD-WI using arrival time differences. The black triangles in (a) indicate the locations of OBNs. This test is used as the benchmark for Fig. S16.

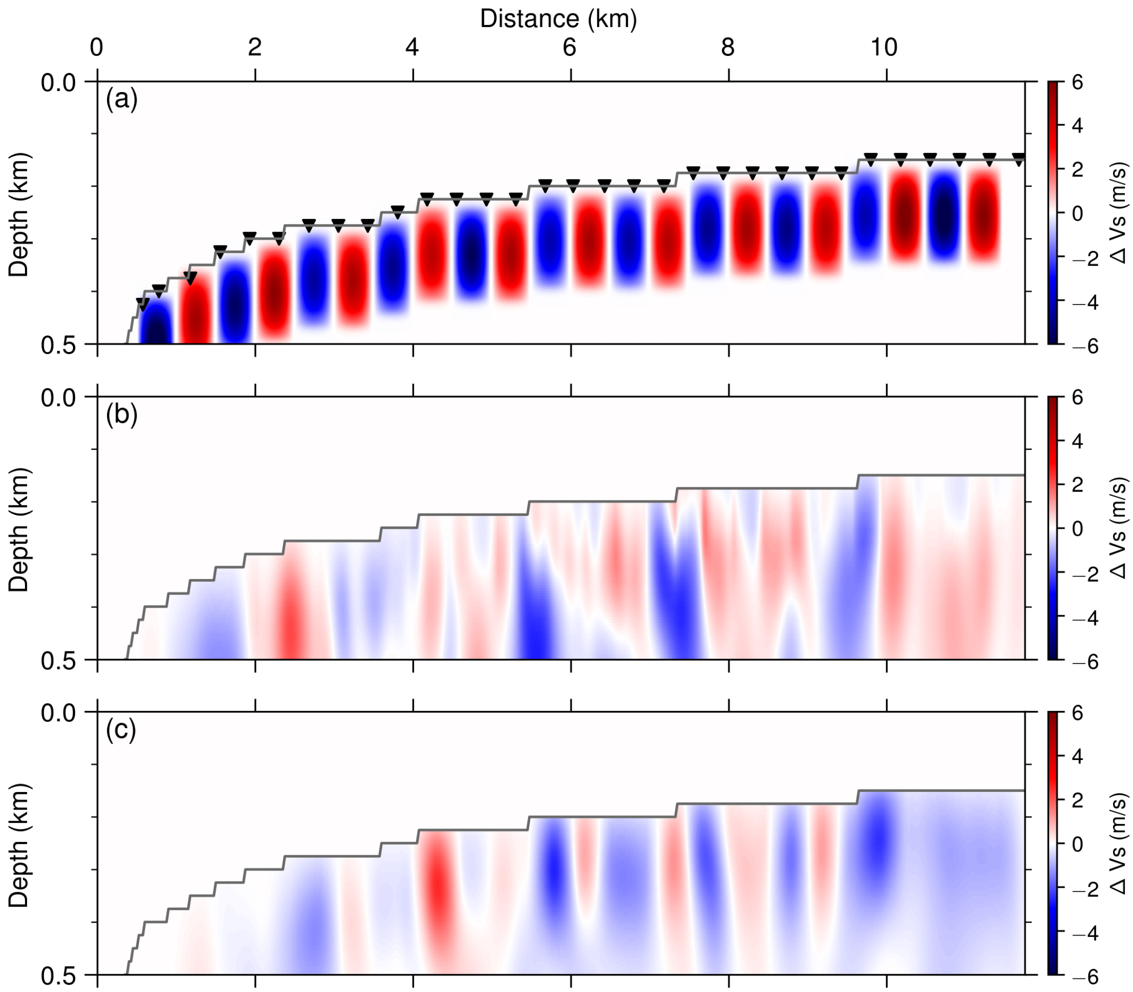

Figure S16. The same with Fig. S15, except that instead of starting DD-WI from the 'true' baseline model (Fig. 4a), we use the model in Fig. S3a as the starting model for DD-WI. The model difference between Fig. S3a and Fig. 4a are much larger than the added velocity anomalies. (a) The true velocity anomalies, (b) the inverted velocity anomalies from DD-WI using waveform differences, and (c) the inverted velocity anomalies from DD-WI using arrival time differences.